

En masse scanning and automated surfacing of small objects using Micro-CT

Riley C. W. O'Neill^{1*}

oneil571@umn.edu

OrcidID: 0000-0001-7492-2540

Katrina Yezzi-Woodley²

yezz0003@umn.edu

OrcidID: 0000-0001-7745-8069

Jeff Calder¹

jwcalder@umn.edu

OrcidID: 0000-0002-9829-4128

Peter Olver¹

olver@umn.edu

OrcidID: 0000-0001-6209-8777

¹*School of Mathematics, University of Minnesota, Minneapolis, MN, USA*

²*Department of Anthropology, University of Minnesota, Minneapolis, MN, USA*

Abstract

Modern archaeological methods increasingly utilize 3D virtual representations of objects, computationally intensive analyses, high resolution scanning, large datasets, and machine learning. With higher resolution scans, challenges surrounding computational power, memory, and file storage quickly arise. Processing and analyzing high resolution scans often requires memory-intensive workflows, which are infeasible for most computers and increasingly necessitate the use of super-computers or innovative methods for processing on standard computers. Here we introduce a novel protocol for en-masse micro-CT scanning of small objects with a *mostly-automated* processing workflow that functions in memory-limited settings. We scanned 1,112 animal bone fragments using just 10 micro-CT scans, which were post-processed into individual PLY files. Notably, our methods can be applied to any object (with discernible density from the packaging material) making this method applicable to a variety of inquiries and fields including paleontology, geology, electrical engineering, and materials science. Further, our methods may immediately be adopted by scanning institutes to pool customer orders together and offer more affordable scanning. The work presented herein is part of a larger program facilitated by the international and multi-disciplinary research consortium known as Anthropological and Mathematical Analysis of Archaeological and Zooarchaeological Evidence (AMAAZE). AMAAZE unites experts in anthropology, mathematics, and computer science to develop new methods for mass-scale virtual archaeological research. Overall, our new scanning method and processing workflows lay the groundwork and set the standard for future mass-scale, high resolution scanning studies.

Keywords: 3D scanning, high-resolution, automated, mass-scale, bones

Statements and Declarations:

Competing interests: the authors declare no competing interests.

*corresponding author

1 Introduction

3D modeling via high-resolution scanning is becoming prolific within archaeological research and, more broadly, anthropological research. This has enabled the development of new data extraction techniques and the application of computationally intensive analyses and machine learning (e.g. [Calder et al., 2022](#); [Göldner, Karakostis, & Falcucci, 2022a, 2022b](#); [Hipsley, Aguilar, Black, & Hocknull, 2020](#); [Hostettler et al., 2024](#); [McPherron, Archer, Otárola-Castillo, Torquato, & Keevil, 2022](#); [Muller, Sharon, & Grosman, 2024](#); [Orellana Figueroa, Reeves, McPherron, & Tennie, 2021](#); [Schunk et al., 2023](#); [Spyrou et al., 2022](#); [Wyatt-Spratt, 2022](#); [Yezzi-Woodley et al., 2021](#); [Yezzi-Woodley, Calder, Sweno, Siewert, & Olver, 2022](#); [Yezzi-Woodley et al., 2024](#)).

Scanning multiple objects simultaneously using computed tomography (CT) scanners previously required tremendous computing power, memory, and time-consuming manual segmentation done by humans. [Hipsley et al. \(2020\)](#) developed a batched micro-CT scanning protocol by arranging straws filled with very small objects in a 50 ml tube. Using their method, 80-253 small objects (<1cm in length) can be scanned simultaneously. Yet, all post processing is manual and was done in proprietary software - manually segmenting, naming, and saving objects with the corresponding identifier using hand-drawn, labeled diagrams for each scan ([Hipsley et al., 2020](#)). They note that as the packing number increases, the packaging tend to shift and not align with the diagram. Concurrent developments by [Göldner et al. \(2022a\)](#) and [Yezzi-Woodley et al. \(2022\)](#) were among the first protocols developed within archaeology for mass scale micro-CT and CT scanning of larger objects. [Göldner et al. \(2022a\)](#) introduced a mass-scale micro-CT scanning and surfacing protocol for lithics. Two sides of a styrofoam block are manually carved out to fit each each object, recording the side, row, column, and identifier for each object. After scanning, the scan is cleaned, surfaced, segmented into each side, segmented into each row, segmented into each object, then saved after entering the correct identifier for the file name ([Göldner et al., 2022b](#)). All of this postprocessing is again manually done by a human and, in part, uses proprietary softwares. While [Göldner et al. \(2022b\)](#)'s advancement makes the scanning process itself much more efficient, the tremendous amount of manual human intervention required in post-processing is very time-consuming, repetitive, and exhausting. The initial surfacing and cleaning here likely requires a computer with large memory (RAM) to be able to operate on the entire scan simultaneously, making it infeasible to run on most consumer-grade computers. In contrast, [Yezzi-Woodley et al. \(2022\)](#) introduced an automated workflow for batched medical CT scanning. This utilizes an automated post-processing workflow designed to scan and surface objects packed in a row with space separating them. Maintaining a CSV file describing the object identifiers (e.g. accession number) and scan layout, the row of objects can be automatically segmented into individual surfaces with the correct identifiers ([Yezzi-Woodley et al., 2022](#)). However, medical CT scanning doesn't offer the resolution of micro-CT, and this doesn't allow the most efficient usage of the scanning bed. Further, both of these packing methods are not very reusable. Naturally, this incentives similar, mostly-automated, reusable, and user-friendly workflows for batched micro-CT scanning of several objects. Indeed, the continued development and extension of such high-throughput scanning methods is paramount to the implementation and innovation of new data extraction and processing pipelines from large 3D mesh datasets.

Here we introduce a new, fully-replicable protocol for mass scale scanning of small objects using micro-CT. Packaging specimens for scanning is low-cost, efficient, and user-friendly. In contrast

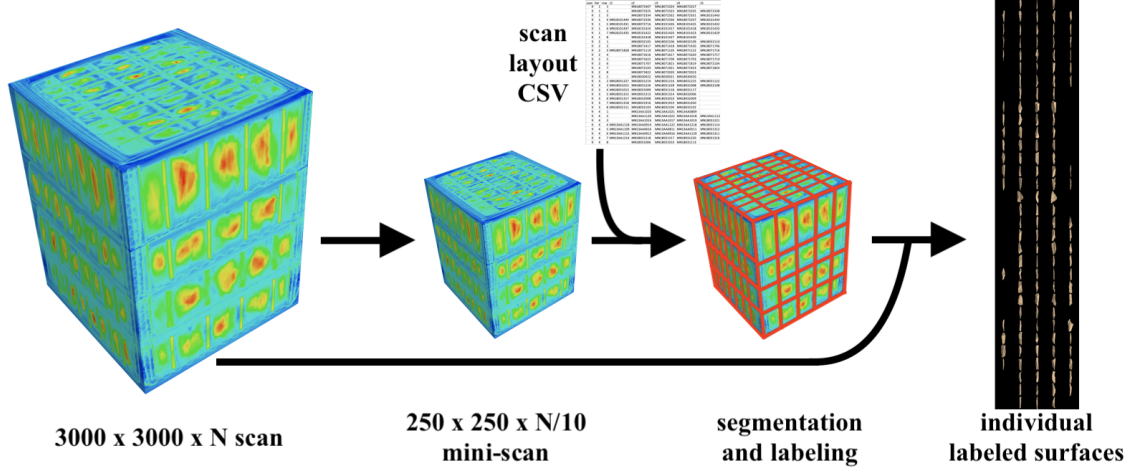


Figure 1: Overview of our processing workflow.

to previous en-mass micro-CT protocols, the segmentation workflow (shown in [Figure 1](#)) requires minimal human intervention to process the scans (only a few minutes per scan as opposed to a few hours). Our method overcomes numerous memory constraints so it runs on any computer with at least 16GB of RAM, removing the need for expensive computational resources. Additionally, our method demonstrates drastic cost and time savings. This method has the potential to revolutionize the scanning of large collections - not just in archaeology, but beyond. In addition to use by other mass-scale high-resolution scanning studies to scan many different materials, our protocol may be adopted by scanning centers to drastically lower the cost of high-resolution scanning by pooling several customers' orders together, making this method effective for any discipline or project where numerous objects can be scanned by micro-CT. Furthermore, our processing code is open access and freely available via the [AMAAZE website](#) and [Github](#), and we will begin to make our models available on an open-access database by the end of 2024.

2 Materials and Methods

2.1 Sample

Bone fragments ($N = 1,151$) were acquired from a collection of experimentally broken appendicular long bones from various ungulates including cow (*Bos taurus*), horse (*Equus caballus*), sheep (*Ovis aries*), elk (*Cervus canadensis*), and deer (*Odocoileus virginianus*). Some bones were broken by people (mostly graduate and undergraduate students) using stone tools to emulate a way early hominins may have broken bones using a hammerstone and anvil or simply by striking the bone against the rock that was used for the anvil. Others were fed to spotted hyenas (*Crocuta crocuta*) at either the Milwaukee County Zoo or the Irvine Park Zoo, both in Wisconsin. The subsequent fragments were submerged in water and cleaned at low heat using crockpots then set out to air dry prior to scanning (See [Coil, Yezzi-Woodley, & Tappen, 2020](#); [Yezzi-Woodley et al., 2021, 2024](#), for a more detailed descriptions of the protocols used for acquiring the physical bone fragments.). The fragments used in this study had a maximum length of 7.27 cm, maximum width of 2.55 cm and height of 1.46 cm (smallest axis of the overall bounding box). The complete list of specimens

can be found in [Table 2](#) in Supplemental Information.

2.2 Packing and Imaging

A total of 1,153 bone fragments were scanned. Fragments were packed into corrugated AVIDITI brand cardboard boxes (9"L x 4"W x 4"H). A package of 25 boxes costs ~ \$27.00 USD through Amazon. Each fragment was placed into an individual cell created by interlocking plastic drawer dividers. A package of 40 Flytianmy brand drawer dividers can be purchased from Amazon for \$22.99 USD. Each interlocking piece is 2.76 inches tall and 12.6 inches long but can be cut into shorter pieces (see [Figure 2 A](#)). The height of each divider dictated the allowable length of the fragment. The way in which the dividers were interlocked dictated the allowable width and depth of each fragment. One interlocking grid of dividers constituted a tier. One to four tiers were placed in each box, stacked one on top of the other and separated by a thin piece of cardboard (see [Figure 2 B](#)). Each tier contained up to 40 fragments and each box contained between 30 and 228 fragments, as shown in full in [Table 1](#). A total of 10 boxes were individually scanned. Handwritten labels were placed on the exterior of each box to ensure that they were properly oriented on the scanning bed.

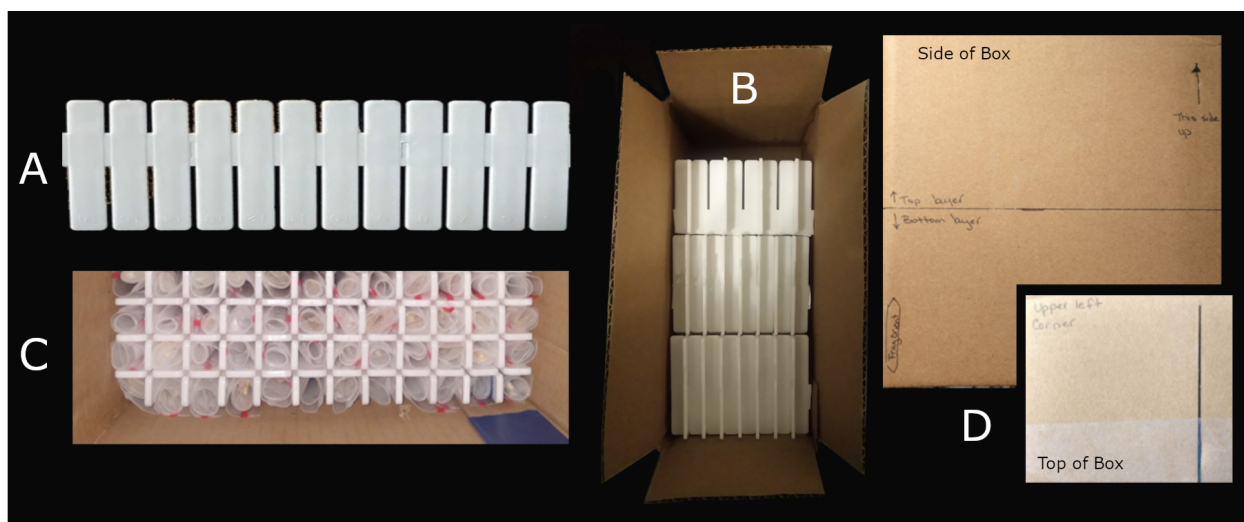


Figure 2: **A** is the plastic divider. **B** is a side view of the scan as it would be placed on the scan bed. Note that the topmost tier is shorter than the other two tiers, demonstrating one way the sizing can be altered to accommodate different sized objects. The extra space at the top of the package was to ensure everything would be captured during scanning. **C** is a bird's-eye-view of a portion of tier. You can see how each fragment is rolled in its plastic bag and inserted into one of the cells. The cell lengths and widths may be varied by adjusting the divider placement and skipping slots. **D** shows labeling on the side and top of the box so that it was clear how the box needed to be set on the scan bed and how it related to the CSV.

The fragments are small (max length 7.27 cm) and thus are curated separately in individual plastic bags. In most cases, the fragments remained in their collections bag which was rolled up and inserted into the cell (see [Figure 2 C](#)). In some cases this would create too much bulk and the

Scan	Fragments (N)
1	228
2	30
3	86
4	134
5	134
6	102
7	109
8	101
9	133
10	96

Table 1: Number of objects (bone fragments) in each scan.

fragment had to be removed from its bag. In these cases, extra care was taken to ensure that the fragment did not become permanently detached from its label. This was done either through careful note taking and/or including a handwritten label in the cell. The outside of the box was labeled with the appropriate orientation (see [Figure 2 D](#)). After the first scan, the box size was reduced to the size provided herein and, in some cases, extra space was left at either the top or the bottom of the box as can be seen in [Figure 2 B](#). The purpose of this was to ensure all objects would be within the field of view and not cut off in the scan.

During the packing process, the arrangement of the objects within each scan was documented in a CSV file we refer to as the "scan layout." Our post processing algorithm crossreferences this essential document to retrieve the object identifiers to properly name the 3D model file of each scanned fragment. [Figure 3](#) shows an excerpt of this CSV file for a 4-tiered scanning package. The first column denotes the scan number (so as to differentiate it from others within the same CSV), and the second column the tier. If looking at rows of the same tier number, it gives an overhead image of the arrangement of fragments within the tier - this is essential to recovering the identities of the constituent fragments. While each tier could hold up to 40 fragments, at least 2 cells in each tier were left empty to form a unique pattern for each scanning package. This was done to easily recover the scan orientation, rule out mirroring, act as a fail-safe if the scan's identity was somehow lost after scanning, and align the CSV layout and the scan for the segmentation algorithm.

Each box of fragments was scanned using a North Star Imaging X5000 micro-CT scanner with a twin head 225 kV x-ray source and a 3073 x 3889 pixel Dexela area detector, housed at the University of Minnesota's ESci XRCT lab. Each scan took between 1 and 1.5 unsupervised hours.

scan	tier	row	c1	c2	c3	c4	c5
9	1	1		MN18072407	MN18072324	MN18072327	
9	1	2		MN18072325	MN18072323	MN18072335	MN18072338
9	1	3		MN18072334	MN18072332	MN18072331	MN18101443
9	1	4	MN18101444	MN18072330	MN18072336	MN18072337	MN18101434
9	1	5	MN18101431	MN18072716	MN18101426	MN18101425	MN18101432
9	1	6	MN18101437	MN18101424	MN18101417	MN18101418	MN18101433
9	1	7	MN18101435	MN18101422	MN18101420	MN18101423	MN18101429
9	1	8		MN18101428	MN18101427	MN18101430	
9	2	1		MN18032105	MN18032106	MN18032109	MN18032110
9	2	2		MN18071417	MN18071418	MN18071420	MN18071706
9	2	3	MN18071828	MN18071119	MN18071120	MN18071122	MN18071716
9	2	4		MN18071616	MN18071617	MN18071620	MN18071717
9	2	5		MN18071622	MN18071709	MN18071703	MN18071719
9	2	6		MN18071707	MN18071815	MN18071819	MN18072104
9	2	7		MN18072103	MN18071921	MN18071923	MN18071824
9	2	8		MN18071822	MN18072020	MN18072023	
9	3	1		MN18030422	MN18030421	MN18030420	
9	3	2	MN18031227	MN18031219	MN18031216	MN18031225	MN18031122
9	3	3	MN18031015	MN18031226	MN18031228	MN18031008	MN18032108
9	3	4	MN18031013	MN18031009	MN18031118	MN18031117	
9	3	5	MN18031315	MN18031313	MN18031314	MN18032006	
9	3	6	MN18031317	MN18032008	MN18032010	MN18032009	
9	3	7	MN18031318	MN18031916	MN18031919	MN18031920	
9	3	8	MN18032111	MN18032103	MN18032104	MN18032102	
9	4	1		MN13AA1020	MN13AA1021	MN13AA0809	
9	4	2		MN13AA1126	MN13AA1022	MN13AA1018	MN13AA1112
9	4	3		MN13AA1016	MN13AA1017	MN13AA1019	MN18031221
9	4	4	MN13AA1118	MN13AA0914	MN13AA1122	MN13AA1218	MN18031114
9	4	5	MN13AA1109	MN13AA0616	MN13AA0811	MN13AA0511	MN18031312
9	4	6	MN13AA1115	MN13AA0912	MN13AA0916	MN13AA1129	MN18031311
9	4	7	MN13AA1214	MN18031218	MN18031217	MN18031220	MN18031316
9	4	8		MN18031006	MN18031010	MN18031113	

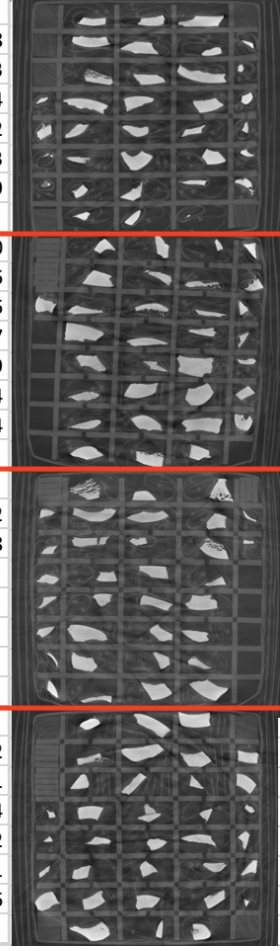


Figure 3: Left: example "scan layout" CSV file for a 4-tier micro-CT scan. Note red lines were added to emphasize different tiers. Each row contains a scan identifier, tier number, row number, and the identifiers corresponding to the objects in that strip of the scan (where present). Right: slices from the corresponding tiers in the scan.

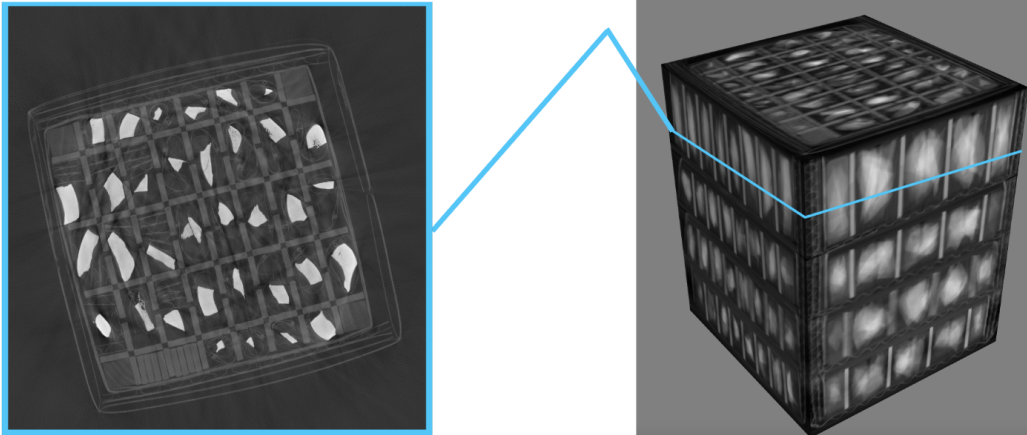


Figure 4: left: a z-slice TIFF image of the scan. Right: visualization of the entire scan.

2.3 Scan Processing

As each micro-CT scan is 70+ GB, some unique challenges arise in processing the scans. For one, an entire scan’s volume cannot be loaded into a conventional computer’s memory. Even the extracted sub-volumes containing each object are several gigabytes. Thus, all scans were stored on a 4 TB drive. To mitigate the memory-usage challenges of the large scans, we developed a semi-automated processing scheme that builds on the work of [Yezzi-Woodley et al. \(2022\)](#). It consists of 5 key steps:

1. **Initial rotation and cropping**, to align the scan with the scan layout CSV.
2. **Subsampling**, to recover a mini-scan that fits in memory for:
3. **Bounding box identification** for each fragment cell (on subsampled volume).
4. **Sub-volume extraction** for each fragment cell (on full scan).
5. **Surfacing** of each fragment via marching cubes and cleaning.

Note that our scans were stored as TIFF *z*-slice images ([Figure 4](#)) on a remote server. Visualizations and bounding-box identification (steps 1 and 3) were done on a 2017 Apple MacBook Pro laptop (250 GB storage, 16 GB memory), while all other operations were done on a System76 machine with a 3960X processor, 48 CPUs, 256 GB Quad channel DDR4 @ 3200 MHz (8x32GB), and 6TB of storage. While all operations can be performed a machine with 16GB of memory, drastic speedups can be obtained with *parallelization*, where processes are divided into smaller tasks that can be run simultaneously over several CPU cores (as opposed to running everything on a single CPU). Most consumer computers do have several CPUs today, but a good-sized memory is required for parallelization to leverage as many cores as possible here. For the most time consuming processes, i.e. sub-volume extraction, surfacing, and cleaning, parallelization contributes to a drastic speedup. Intermediary data and the outputs of steps 1, 2, and 3 were exchanged between the two devices using SSH (SecureShell)¹.

2.3.1 Initial Rotation and Subsampling (Steps 1 and 2)

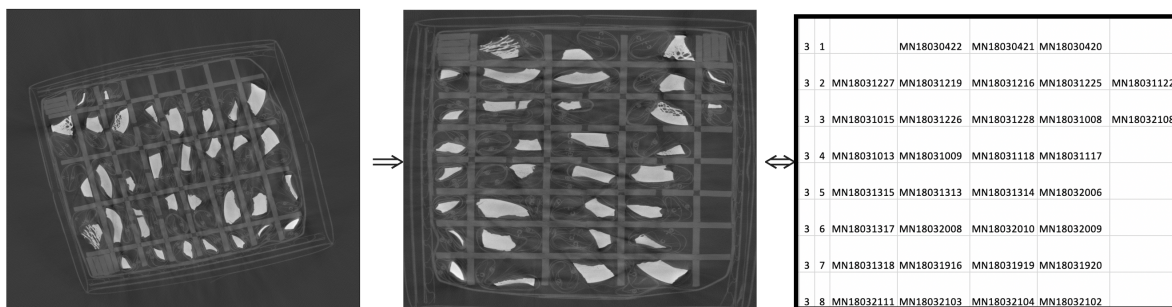


Figure 5: Left: original TIFF image. Middle: cropped and rotated image. Right: CSV layout.

¹Note that portions of our Python code are designed to use SSH and will have logins and passwords redacted prior to publication so as to ensure the security of our server; functionality for portable drives and local files was not the original use-case but has been added for publication.

While the scanning packages were placed on the micro-CT scanning bed following the "this side up" labels (Figure 2 D), no additional alignment was done - they took random positions within the scanning bed, especially regarding rotation in the x - y plane. Thus, 2-6 slices from each scan were manually inspected to align the vertical view with the scan layout CSV via rotation and cropping (the latter simply to remove empty space). As described earlier, fragments were arranged so as to ensure the orientation could be always recovered from their arrangement alone, i.e. cells were selectively left empty to preclude rotational and reflective symmetry. The angle and row and column cropping ranges (start index, stop index) were identified by trial and error; an example is shown in Figure 5. This took only a few minutes for each scan. The 5 identified values were then stored in a text file for each scan. While the original scans could have been cropped, rotated, and saved to reduce data-storage, this was ultimately not done to ensure data fidelity and avoid corruption or other adverse possibilities.

Each TIFF z -slice of the original micro-CT scan was 2952 by 2971 pixels. Rotating and cropping the scan to just the scanning package gave about 2500 by 2500 pixel images for all scans except #1. The scans varied in height (z -direction) - the tallest had $h = 3813$ images. The rotated and cropped scans were subsampled by resizing the z -slices to 225 by 225 images and then averaging together batches of 10 slices (or however many remained at the top of the scan) for a $255 \times 225 \times \text{ceil}(h/10)$. This subsampled grid could be then completely loaded into standard machine memory for bounding box identification.

2.3.2 Bounding Box Identification (Step 3)

Bounding box identification consists of 5 phases: (1) identification of object and divider voxel ranges and thresholding; (2) vertical (z) segmentation into individual tiers; (3) divider detection and automatic tier rotation; (4) automatic rotation; and (5) grid segmentation.

Phase 1: Identification of voxel value ranges and thresholding. While medical CT scanners are finely calibrated so the voxel values of an object directly correspond to its Hounsfield units, micro-CT scanners are not. Quite contrarily, the voxel values of micro-CT scans are extremely sensitive to a variety of scanner and processing settings: KV MicroAmp, table position, detector position, beam hardening, resampling, etc. This means that the voxel values for objects of the same density can vary *wildly* between scans - within our own data, bones started at 17000 in one scan and 38000 for another, with many other values in between. Despite these variations, all the voxel histograms "looked the same" (up to translation), resembling a triple Gaussian. This is shown in Figure 6 - from left to right: one large peak for air/background, a smaller peak for the plastic dividers, and a very low and wide peak for the objects (bones).

Since the placement of the plastic dividers and cardboard delineate the regions to extract and correspondence to the layout CSV, this is exactly what our algorithm uses for segmentation. Thus, it is essential to identify the start and stop of the divider range ($a_{divider}, b_{divider}$). Surfacing later requires the extent of the object of interest range as well (a_{object}, b_{object}); we set $b_{object} = \infty$ since nothing else was denser in the scan. These ranges are shown in Figure 6 (right). Several options were considered for automatic identification of these three values (e.g. triple gaussian fitting, find-peaks), these proved to be sensitive to noise or initialization and struggled to identify the bone range. Instead, manual identification of $a_{divider}, b_{divider}$, and a_{object} took just a few seconds per

scan via a guided-user-interface.

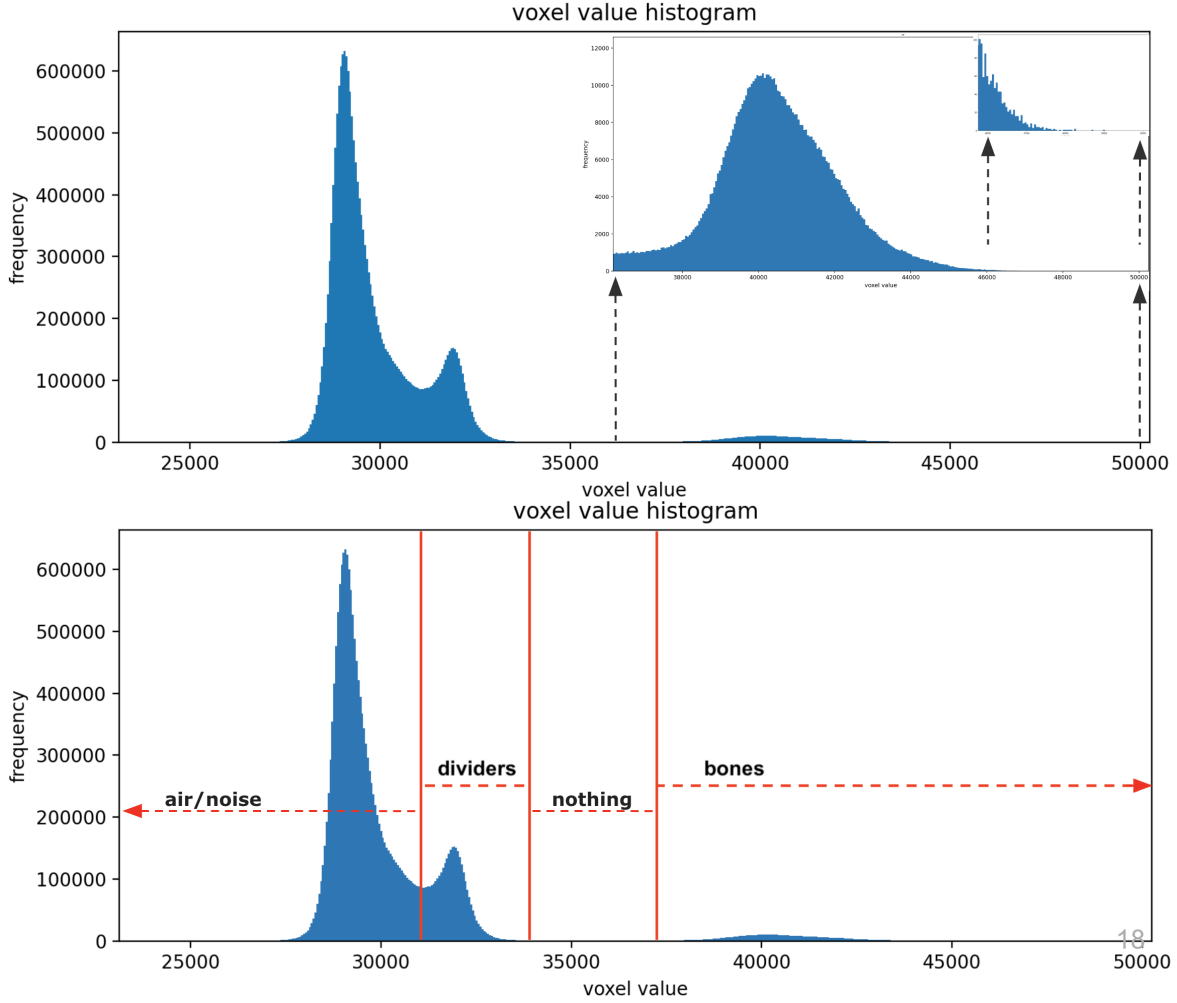


Figure 6: Left: density histogram for total subsampled volume (500 bins). The largest peak corresponds to background (air), the middle peak the cardboard, and the low right peak the bones. Right: 3 user selected threshold values to identify the cardboard range and start of the bone range.

Phase 2: Vertical Segmentation Each tier consists of plastic inserts separating bones, and cardboard separates the tiers. Bone has a higher density than cardboard, so the average pixel value for a z -slice containing only cardboard is lower than that of a tier with plastic and bones. Let D_k be the average pixel value over the k th z -image in the $225 \times 225 \times N$ subsampled volume. Peaks in $-D_k$ then correspond to the tier boundaries. The layout CSV file says how many tiers are in each scan, so we know how many peaks to look for to split the scan. We used an automated peak detection interface (minimum width = 10) with user verification and optional input to ratify or modify the detected peaks for splitting each scan into individual tiers. This is shown in Figure 7.

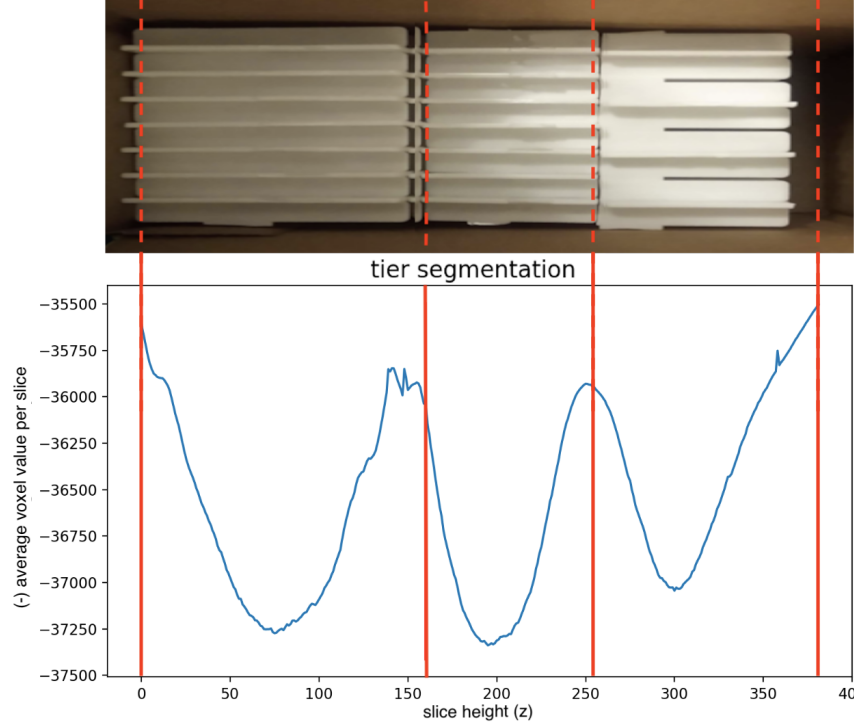


Figure 7: Top: Dividers, side view. Left to right is higher in the scan. Bottom: negative average density for each tiff-image plotted against slice height subsampled volume. Peaks (corresponding to lower densities) denote boundaries between tiers - i.e. how to split the scan, while valleys denote regions with denser material (i.e. bones). Right: segmentation into 4 tiers (user verified). I would make this look like a single figure, trim left margin of photo and extend red lines to arrows. This will mess with the tier segmentation label perhaps.

Phase 3: Divider detection After obtaining the user-input bounds for the divider and object ranges as described in [Section 2.3.2](#), we leverage these ranges to robustly extract the dividers from the tier volume. Let V denote the $225 \times 225 \times H_z$ tier volume, with V_{ijk} a single value and $V_{ij} = [V_{ij1}, \dots, V_{ijH_z}]$ a vertical segment. We want to extract a 225×225 image denoting where the dividers are. A simple yet effective way is to count how many pixels of V_{ij} are in the divider/cardboard range and subtract how many pixels in V_{ij} are in the object range, i.e.:

$$I_{ij} = \#\{k : a_{divider} \leq V_{ijk} \leq b_{divider}\} - \#\{k : a_{object} \leq V_{ijk} \leq b_{object}\}$$

This is quite intuitive: the divider boundaries should not sit under/over bones, so very high values are very likely dividers boundaries. Thresholding this image to values within 75% of the maximum value gives very-sure dividers:

$$B_{ij} = \begin{cases} I_{ij}, & \text{if } I_{ij} > 0.75 \cdot \max_{mn}(I_{mn}) \\ 0, & \text{otherwise.} \end{cases}$$

B is ultimately used for automatic rotation and chopping the tier. An example is shown in [Figure 8](#).

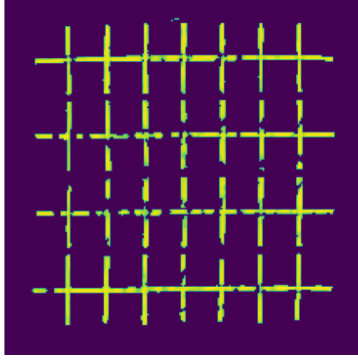


Figure 8: Detected cardboard dividers for tier 1.

Phase 4: Automatic Rotation of Tiers

Once the subsampled volume has been chopped into individual tiers, it needs to be segmented into individual bounding boxes. Since we used drawer dividers stacked atop one another, the tiers do not always align squarely with one another: in some instances they slightly twist, so we developed a method to automatically rotate them (by small angles) so identifying the bounding boxes becomes very simple.

The automatic rotation works on the single divider image per each tier (B , as constructed above). It seeks to maximize the horizontal/vertical detail to diagonal detail ratio. Define

$$V = \begin{bmatrix} 1 & -1 \\ 1 & -1 \end{bmatrix}; \quad H = \begin{bmatrix} 1 & 1 \\ -1 & -1 \end{bmatrix}; \quad D = \begin{bmatrix} 1 & -1 \\ -1 & 1 \end{bmatrix}$$

and $R_a(I)$ the image rotated a degrees using bilinear interpretation. We want to maximize

$$J(a) = \frac{\sum_{i,j} (V * R_a(B))_{ij} + (H * R_a(I))_{ij}}{\sum_{i,j} (D * R_a(I))_{ij}}$$

over a small interval of angles, e.g. $a \in [-10, 10]$, which was done via sampling an evenly spaced partition in increments of $1/10$. An illustration of this completely automatic process is shown in [Figure 9](#).

The method works very well for the crisp divider images (B) for each tier. We originally considered applying it to the z average of voxel values for each tier, but this was far less robust due to the presence of high-magnitude non-grid objects. In theory, J should be smooth in a and resemble a sinusoid. Experimentally, the numerical implementation of the bilinear interpretation gave some noise resembling Gibbs phenomenon about $a = 0$, irrespective of attempts to counteract the issue. We resolved to smooth J and perform a quadratic fit to identify the maximum, which experimentally worked well.

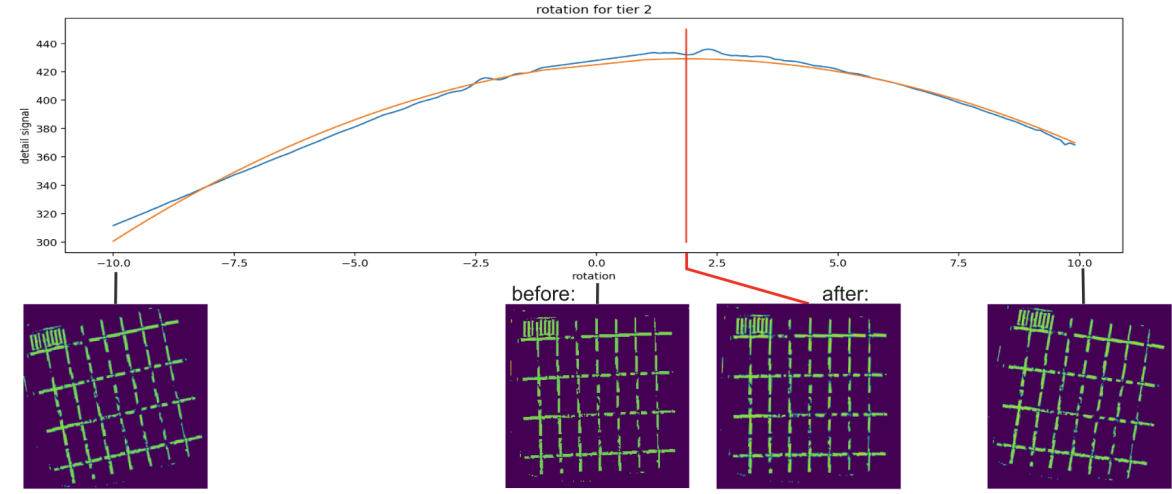


Figure 9: Automatic rotation. Top: vertical/horizontal to diagonal detail ratio (J) plotted in blue against the angle of image rotation θ in degrees. Angles were sampled every 0.1 degrees between -10 and 10. Due to noise about the peak, a quadratic fit (orange) was performed to find the peak rotation angle. Middle left: detected tier dividers image before rotation ($\theta = 0$). Far left: $\theta = -10$. Far right: $\theta = 10$. Middle right: output image corresponding to detected peak response from quadratic fit (about 1.9 degrees here).

Phase 5: Grid Segmentation was done by summing the final rotated B image along the x and y axes and identifying peaks, as shown in Figure 10. The CSV file conveys how many rows and columns there are, i.e. how many peaks we should seek for each tier. Extracting the box coordinates corresponding to nonempty cells in the CSV file and storing and rescaling the various crops and rotations along the way, we can then extract the fragments from the original scan.

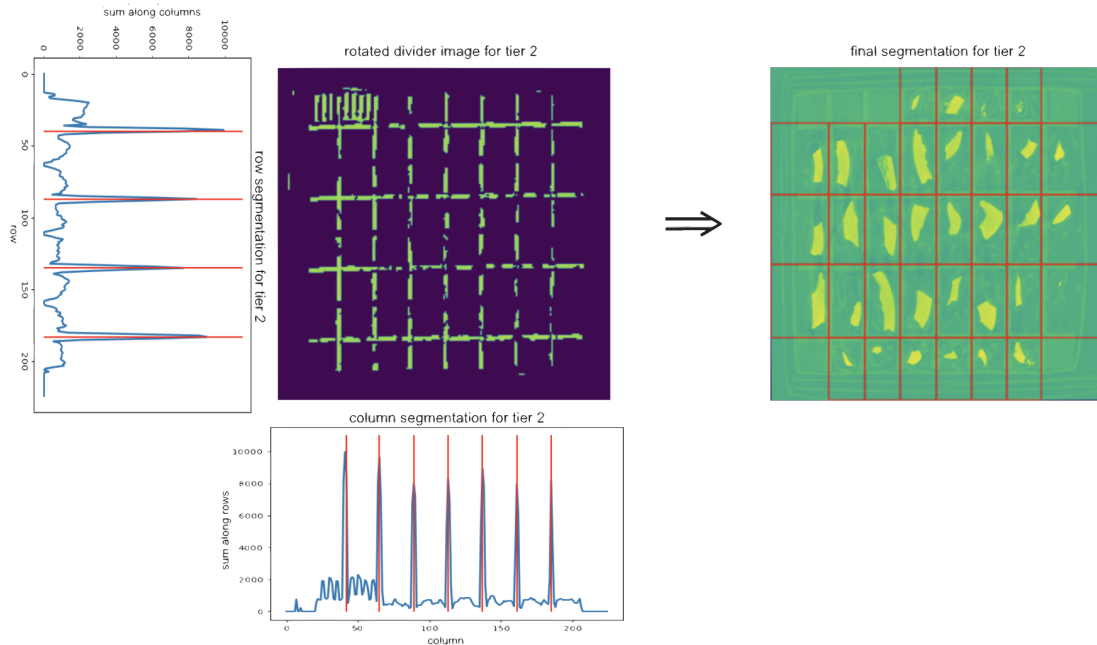


Figure 10: Final grid segmentation for a single tier.

2.4 Bounding box extraction, marching cubes, and cleaning

The extracted bounding boxes were padded slightly so as to prevent possible truncating of any fragments. Due to memory constraints, this was done by looping over each object in the scan and extracting and storing the sub-array corresponding to the box coordinates. This is by far the most time-consuming part of the runtime, but is readily accelerated with parallelization. Surfacing was initially done using marching cubes with the second user-identified threshold (upper limit of cardboard range) as the input isolevel (the voxel value that objects will be at or above), and revised to a different isolevel if needed. Finally, the output meshes were cleaned. This was done by keeping the largest connected component without holes. Other approaches to cleaning may suit other tasks.

3 Results

From 1,153 objects packed into just 10 scanning packages, we successfully scanned, processed, and surfaced 1,112 objects in entirety to a resolution of 41.8 - 56.0 μm . The resolution varied slightly from scan to scan. The disparity in the number of objects comes from the first (trial) scanning package being too large for the scanner's field of view. This means some objects were not completely in the scan, as discussed more in [Section 4.2.2](#); all other 9 scans fit within the field of view, and all objects in them surfaced successfully and in entirety. By packing the objects into a tiered 3D grid structure and creating CSV files that track the layout and identifier of objects in each tier, the scans were successfully segmented into individual cells and then surfaced into individual object PLY files with the correct object identifiers.

Scan packaging and documenting the layouts in a CSV file took about 30-45 minutes per scan. Each scan took 1-1.5 hours to complete, and preliminary post processing (manual) took 30 minutes per scan (done concurrently with scanning). The final segmentation and surfacing workflow was almost completely automated, requiring under 10 minutes of manual human intervention in just the early portion of the workflow (only steps 1 and 3; steps 4-5 are the bulk of the runtime). These algorithms took less than 4 hours to run (unparallelized), or 1-1.5 hours parallelized on a more advanced computer. Thus, to scan our entire sample of 1,112 fragments, it took 25-38 hours, of which only 11-14.5 hours required manual human interaction. This averages to 1.1-1.5 hours of manual human work per each scan (average of 115 objects in each). This is 35 seconds of human time per object and about 2 minutes total per object. [Figure 11](#) showcases some of our resulting bone surfaces.

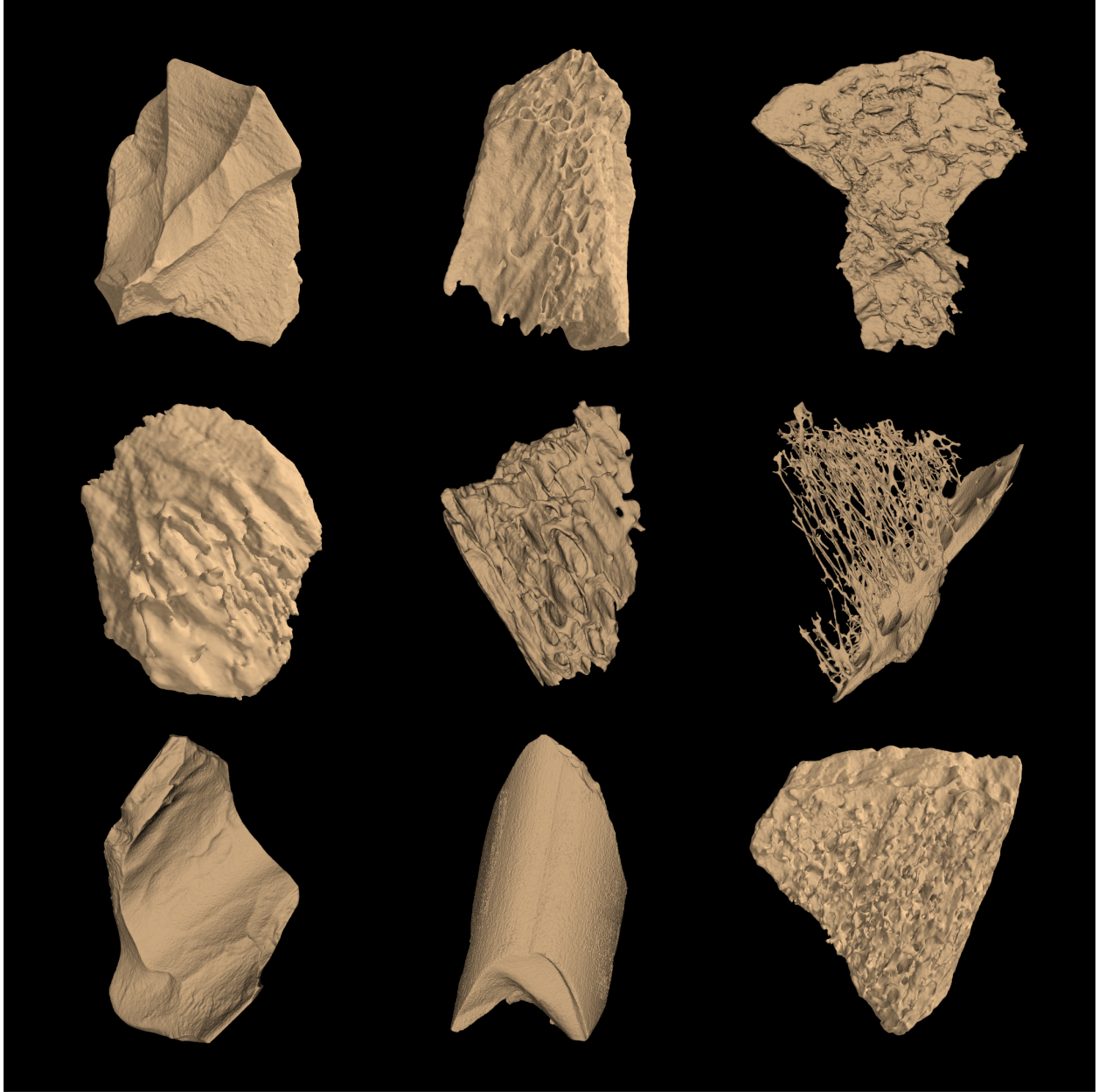


Figure 11: Final micro-CT surfaces of bone fragments, all with $41.8 - 56.0\mu\text{m}$ resolution.

4 Discussion

4.1 Important Considerations When Scanning

There is no single scanning method that will be optimal for all projects writ large. In order to choose which method to use when approaching a research project involving 3D surface modeling, there are several inter-related considerations to evaluate. The first level of consideration pertains to resolution and sample size. The sample size needs to be sufficiently large to address the research question and that the resolution of the 3D models must capture the detail necessary to address

the research question. Once this is decided, attention can turn to the details of each stage of the workflow. Broadly, these stages are: preparing objects for scanning; scanning; processing data and surfacing scans; utilizing the 3D models for research; and curation of all data and metadata. The final major consideration is replication and reproducibility. The cost/benefit analysis can be thought of in terms of time (interactive and automated), money, human resources, required skill sets, location, materials, and scanning and computer hardware and software.

4.1.1 Resolution and Sample Size

The use of high resolution scanning introduces challenges relating to data-structures (file format), computer memory and processors, storage, and processing time especially as it pertains to working with larger samples. For example, during processing, a typical scan from this project required 62 GB for just the TIFF images (scan slices), and all 10 scans' slices required 615 GB in total. With the associated scan metadata, final object surface PLY files, and intermediary NPZ subvolumes (compressed Numpy arrays) and other metadata produced by our workflow, this project consumed 2.7 TB of storage. While it is not essential to keep the NPZ subvolume files (2-6GB each) and just keep the output PLY surface files (8-64 MB each), we elected to for possible downstream tasks. All of this was stored on a 4TB drive for portability. Unlike previous work, our workflow never brings the entire scan into machine memory for processing. Paired with the portable drive, this allows our workflow to run on any standard consumer-grade computers with at least 16GB of memory (provided the extracted object sub-volumes are less than this - more on that momentarily). This allows those without access to intensive computing resources but still access to micro-CT scanning and suitable storage space to use our methods.

Subvolume extraction and surfacing via marching cubes are by far the most memory-intensive and time-consuming parts of our workflow, as these perform many operations on full-resolution subvolumes. After some experimentation to find the fastest procedure, we implemented a single slice reading loop where subvolume files are incrementally appended *in-disk* as opposed to *in-memory* using the recent `numpy.append_array` module [Siebert, Adelman, and Git \(2023\)](#). Appending these subvolume arrays in-disk as opposed to in-memory eases memory constraints, allowing one to scan larger objects as well (e.g. 4 large objects as opposed to 150 small objects). Sub-image extraction and writing may be parallelized within the reading loop for faster execution. Unparallelized, the runtime for this took 3 hours for a representative scan, and one should expect even faster times if parallelizing the inner image-writing loop.

Surfacing via marching cubes was parallelized as well for faster execution, wherein each worker loads a subvolume into memory and surfaces it. Here we find the ultimate memory bottleneck of our workflow: the entire subvolume must fit comfortably into memory with room for performing the marching cubes algorithm. Most of our subvolumes were on the order of 5GB; for 16GB memory machines, parallelization is less tractable, and this can be time consuming. For machines with much larger memory and more CPUs, again parallelization contributes to a substantial speedup. For applications with relatively large objects at high resolutions (e.g. 16GB / object bounding box) and computers with limited memories (e.g. 16GB), ultimately a different approach to surfacing must be utilized, but we did not encounter this problem.

4.1.2 Workflow Considerations

In order to prepare the physical objects for scanning, the first consideration is whether sample can be transported to the scanner or, if the scanner needs to be transported to the sample. In this case, we transported the objects to a large, fixed scanner. Portable micro-CT scanners are still extremely rare, though there are bench or desktop micro-CT and XRM scanners available through companies such as Bruker. Perhaps such a scanner could be purchased for permanent use at a field site but transporting the scanner back and forth might not be feasible. For example, one of Bruker's smaller XRM scanners, the SKYSCAN 1275, weighs 170 kg (340 lbs).

However, the ability to transport the collection to the scanner can save the overall time investment and financial expenditures. Several hundred small objects can be scanned simultaneously using our method: scanning 150 objects individually with micro-CT would require more preliminary post-processing time overall and cost several thousand dollars (\$15,000 if for an hour each at our rates), but packing these together for a single scan with our method would cost only \$150. Further, the materials used for packaging the physical objects for transport and scanning were inexpensive and easy to acquire.

Time is money too, and our method is extremely effective for use of human time, scanner time, and post-processing time. A package of 150 fragments only takes 1-1.5 hours to scan, whilst scanning 150 fragments individually takes well beyond this (not to mention load/unload time and added post-processing time). Our segmentation and surfacing protocol takes under 4 hours to run (unparallelized), and can leverage greater computational resources (i.e. more CPUs and RAM for parallelization) to drastically accelerate this to 1-1.5 hours or less. Only 1-1.5 hours of manual human work were required for each scan (30-45 min packing, 30 min preliminary post processing, and < 10 min of input to the segmentation and surfacing workflow). Furthermore, as we developed this protocol, we experimented with the total number of fragments that could be included in each scan. In retrospect, a maximum of 158 could have been utilized, resulting in an overall sample of 1580 reducing the overall time per object to 90 seconds.

Though micro-CT scanners and scanning are expensive, following our protocol to batch many objects together in a single scan can deliver tremendous cost-savings per object. micro-CT scanners range in price from about \$250,000 to \$1,000,000 and are often purchased for use by many organizational divisions and projects so the costs to individual projects are reduced. Our scans were acquired at the University of Minnesota's XRCT lab, which charged \$150 per scan. The total cost of our 10 scans after packaging materials was \$1,549.99. While this is a large sum of money, with 1,112 objects successfully scanned, the price per object is only \$1.18! If filling to the maximum of 158 objects per scan, this is only \$0.98 /object. Furthermore, once the 3D models are acquired their use life can be extended at no extra cost through use in future projects and via data sharing.

4.1.3 Curation, Replication, and Reproducibility

The capacity to create voluminous amounts of data is only the first step. Handling large amounts of data after-the-fact can be a complex process. This is especially true within archaeology, where researchers must synchronize and work between collections in both their physical form and digital form along with the associated metadata that provides the all-important context necessary in our field. Furthermore, excavation and research at archaeological sites are generally ongoing meaning

that collections (physical and virtual) oftentimes continue to expand over time. The sheer amount of data and metadata can be confusing and overwhelming, especially for those who are accessing these collections with minimal prior experience with either the collections or the methods utilized to create them (e.g. students, early-career researchers, independent research groups, and educators). Such expansion in the sheer amount of data coupled with the goal of optimizing access to broad audiences amplifies the curatorial and infrastructural needs for building organizational frameworks that support the usability of shared data.

Our new Micro-CT protocol offers a simple, (comparatively) affordable, and user-friendly means to package and track objects through the workflow, as well as organize surface data afterward. Provided curatorial standards and object identifiers that can accommodate a growing collection, our packaging and scanning protocols are readily deployable and intuitive. The output surfaces are named with the object identifier and isolevel, which allows easy organization after scanning as well as the user to experiment with multiple isolevels. Each step of our post-processing saves auxiliary meta-data files that track coordinates, rotations, and important thresholds, so the workflow is entirely replicable (and may reuse such values). All our code will be published on the [AMAAZETools Github](#) as well as linked to from [our website](#). Models from this project will be available on request and we aim to begin putting them in an open-access repository by the end of Dec 2024.

4.2 Lessons We Learned Along the Way

The scientific method is inextricable from trial and error. Here we outline some pitfalls we encountered, our workarounds, and means of eliminating such issues in future uses of our protocol.

4.2.1 Voxel Value Distributions and Optimal Isolevels for Surfacing

After scanning and preliminary post-processing, we found that the distribution of micro-CT voxel values varied drastically from scan to scan. Unlike CT scanners, which are calibrated to output Hounsfield units (and which [Yezzi-Woodley et al. \(2022\)](#) used to develop the completely automated CT batch scanning protocol), micro-CT scanners are not calibrated to be in Hounsfield units - the output voxel values are extremely sensitive to a number of parameters for each scan, including KV MicroAmp, table position, detector position, beam padding, and more. This means that the output voxel values can vary wildly between scans, e.g. bones could be 14000-26000 in one scan and 32000-42000 in another, although the two distributions share the same characteristics outlined in [Section 2.3.2](#). As such, it is inordinately difficult to calibrate the output voxel values without some controls in each scan of a known density, e.g. a vial of water. We did not do this, and rather than try to match voxel distributions between scans, we opted for simple manual inspection. However, if placing controls in each scan, this could easily be automated.

Therein, the optimal isolevel for surfacing varies between scan and often requires some trial and error to select. Were the scans calibrated and standardized, it would be easy to specify the isolevel corresponding to the objects' physical density/ies. Surfacing is relatively fast to rerun for each scan, so several values may be inspected to identify the user's preference. The ideal isolevel is very important, especially when one's objects are thin. Thus, in situations where the objects may vary greatly in thickness, it is useful to package together items that have a similar thickness.

4.2.2 Capturing the Entire Specimen

While our first trial scanning package fit on the Micro-CT *scanning bed*, it did not fit in the scanner’s *field of view*. As such, 39 objects from scan 1 failed to yield complete surfaces. Our subsequent packages were smaller to fit within the field of view. When first implementing a high-throughput micro-CT scanning workflow, the scanner’s field of view and corresponding resolution should be ascertained prior to starting scanning so an appropriate package size may be used.

4.2.3 Cell Alignment within Package Tiers

Few objects in this study filled their entire cells. As space is money in this setting, an organizing system with an irregular arrangement of rectangles (e.g. at right in Figure 12) may seem more efficient. While this can be scanned, this will not work with our CSV scan-layout organizational system nor grid detection algorithm. Our protocol needs objects to be arranged in an $N \times M$ grid. The width of each row and column may vary, but the grid lines must go from end to end in the box. An acceptable example of this is shown at left in Figure 12. Therein, it is prudent to organize like-sized objects together before packing so one may get the maximal number in a given scan.

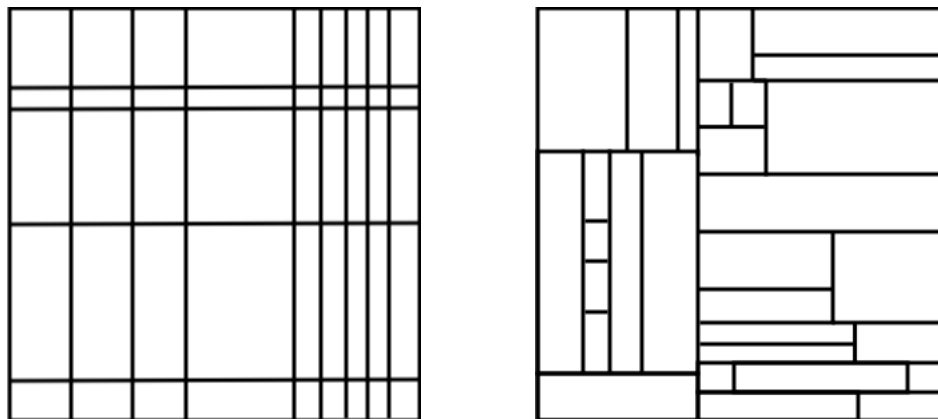


Figure 12: Examples of acceptable and unacceptable tier arrangements. Left: an acceptable grid arrangement for our protocol. Objects are arranged in an $N \times M$ grid; the width of the rows and columns may vary within a tier, and the number of rows and columns may vary between tiers in the same scan. Right: while this may be acceptable as a Mondrian inspired design, it is an unacceptable grid arrangement for our protocol. Grid lines must go side to side and yield an $N \times M$ arrangement to store and recover the object identities.

Note that the number of rows (N) and columns (M) need not be fixed for all tiers in a given scan, and indeed the tier height may vary as well, allowing for more flexible and efficient scanning. For all but one of our scans (CT 1), we used the same grid arrangement for all tiers. Crucially, if electing for variable N and M within the same scan, the number of rows and columns should also be stored for each tier in the scan-layout CSV file so as to enable our fully automated grid recognition code. This would require but a minor modification to our code and previously presented scan layout CSV arrangements.

4.2.4 Future Research and Applications

Future research largely spans ways to make the algorithm completely automated and more efficient. As discussed in [Section 4.2.1](#), known density controls (e.g. vials of air or water) could be placed in the scan to calibrate the output voxel distribution. This could make bounding box identification and scan orientation completely automatic and give known isolevels corresponding to the objects of interests' density. Further, an interlocking 3D tier grid would remove the need for automatic tier rotation, and remove some tier-wise operations as well. More advanced or automatic methods for isolevel selection merit exploration as well.

As to future applications, our protocol rapidly increases capacities for scanning large scale archaeological and paleontological collections, enables broader access to materials by independent research teams, promotes digital curation and expanding public outreach in museum settings, invites increasingly robust applications using methods such as machine learning and deep learning, and opens pathways for advancing digital data extraction within archaeology. Furthermore, our protocol and workflows may be immediately adopted by scanning institutes, centers, and companies to batch several customers' orders together and achieve lower scanning cost, e.g. closer to \$0.98/object opposed to \$150 for scanning an object individually. This would mark a tremendous development for 3D modeling and democratize high-resolution scanning. Our protocol also works at a larger scale as a means for en-masse CT scanning, where a human-sized box or several boxes can be used to pack hundreds to thousands of objects. Further, as our workflow applies to any objects with a density discernible from the dividers and cardboard, a plethora of objects beyond bones may be scanned, including lithics, ceramics, metals, glass, circuits, and more. Therein, many other fields may immediately apply our methods to implement their own mass-scale micro-CT or CT scanning studies.

5 Conclusion

Our new en masse micro-CT scanning protocol offers a novel and efficient means for obtaining 3D models for hundreds, if not thousands, of small objects from a single scan. From only 10 micro-CT scans, we successfully obtained high resolution 3D models for 1,112 objects at a cost of just \$1.40 USD each, or \$0.98 USD if we had packed them to the fullest. Building off previous semi-automated approaches to batched medical CT scanning ([Yezzi-Woodley et al., 2022](#)), our work here offers hassle free packaging, mostly automated and memory-efficient post-processing with minimal human intervention, and tectonic cost and time savings all around. Notably our post-processing workflow runs on any computer with at least 16GB of RAM, taking less than 4 hours per scan on 1 CPU. This enables those with sufficient storage but limited computational resources to still use our methods, therein making high-resolution scanning more accessible. With more CPUs and RAM, the memory-intensive parts of our workflow are easily parallelizable to deliver runtimes on the order of 1-2 hours per scan, therein increasing the accessibility to high-resolution scanning. While human intervention in post-processing takes less than 10 minutes per scan, we outlined ways to make post-processing fully automated. Likewise, automated scan packaging and labelling could be done for industrial applications.

As our method works for any objects with densities discernible from the cardboard and plastic

dividers, it applies to innumerable types objects (provided the objects all fit within the chosen grid system and scanner’s field of view). Therein, this bears immediate applications in numerous fields, including paleontology, geology, engineering, materials science, and manufacturing. Our [open-source code repository](#) and convenient packaging protocol allows our method to be rapidly adopted for such applications.

Beyond use for en masse micro-CT scanning, our protocol immediately works as a method for en masse medical CT scanning. Several boxes or a single human-sized box packed in the same way we described may be scanned to surface tens of thousands of objects simultaneously. In addition to use by other mass-scale micro-CT or CT scanning studies, our method may also be adopted by micro-CT scanning centers to batch several customers’ orders together and scan them simultaneously. This would offer tremendous consumer cost savings, greater efficiency, reduced power usage, and greater accessibility to high-resolution models for all.

As our world is increasingly digital and studies demand increasingly higher resolution data, increased efficiency and accessibility of micro-CT scanning are paramount. Here, we introduced a new, scalable, open-source method for mass scanning that enhances researchers’ ability to leverage high-resolution data. This approach not only benefits anthropology but across disciplines in a way that democratizes access to advanced research using micro-CT and offers a significant leap in efficiency within archaeology, a discipline that uses extensive material collections.

6 Acknowledgments

RCWO was supported by NSF GRFP-2237827 and NSF-DMS:1944925, KYW was supported by NSF SPRF-2204135, and JC was supported by NSF-DMS:1944925 and NSF-CCF:2212318. We are grateful to insightful conversations with John Brigham of the University of Minnesota Visible Heart Laboratories. The bones were acquired from Scott Salonek with the Elk Marketing Council and Christine Kvapil with Crescent Quality Meats. Bones were broken by hyenas at the Milwaukee County Zoo and Irvine Park Zoo in Chippewa Falls, Wisconsin or by various math and anthropology student volunteers who broke bones using stone tools. Abby Brown and the Anatomy Laboratory in the University of Minnesota’s College of Veterinary Medicine provided the facility to clean bones fragments. The bone fragments are curated by Matt Edling and the University of Minnesota’s Evolutionary Anthropology Labs. The fragments were scanned at the Department of Earth and Environmental Sciences XRCT lab with the guidance of Francesca Socki.

References

- Calder, J., Coil, R., Melton, J. A., Olver, P. J., Tostevin, G., & Yezzi-Woodley, K. (2022). Use and misuse of machine learning in anthropology. *IEEE BITS the Information Theory Magazine*, 2(1), 102–115.
- Coil, R., Yezzi-Woodley, K., & Tappen, M. (2020). Comparisons of impact flakes derived from hyena and hammerstone long bone breakage. *Journal of Archaeological Science*, 120, 105167.
- Göldner, D., Karakostis, F. A., & Falcucci, A. (2022a). Practical and technical aspects for the 3d scanning of lithic artefacts using micro-computed tomography techniques and laser light

- scanners for subsequent geometric morphometric analysis. introducing the styrostone protocol. *Plos one*, 17(4), e0267163.
- Göldner, D., Karakostis, F. A., & Falcucci, A. (2022b). Styrostone: A protocol for scanning and extracting three-dimensional meshes of stone artefacts using micro-ct scanners. *Protocols.io*.
- Hipsley, C. A., Aguilar, R., Black, J. R., & Hocknull, S. A. (2020). High-throughput microct scanning of small specimens: preparation, packing, parameters and post-processing. *Scientific reports*, 10(1), 13863.
- Hostettler, M., Buhlke, A., Drummer, C., Emmenegger, L., Reich, J., & Stäheli, C. (2024). *The 3 dimensions of digitalised archaeology: State-of-the-art, data management and current challenges in archaeological 3d-documentation*. Springer Nature.
- McPherron, S. P., Archer, W., Otárola-Castillo, E. R., Torquato, M. G., & Keevil, T. L. (2022). Machine learning, bootstrapping, null models, and why we are still not 100% sure which bone surface modifications were made by crocodiles. *Journal of Human Evolution*, 164, 103071.
- Muller, A., Sharon, G., & Grosman, L. (2024). Automatic analysis of the continuous edges of stone tools reveals fundamental handaxe variability. *Scientific Reports*, 14(1), 7422.
- Orellana Figueroa, J. D., Reeves, J. S., McPherron, S. P., & Tennie, C. (2021). A proof of concept for machine learning-based virtual knapping using neural networks. *Scientific Reports*, 11(1), 19966.
- Schunk, L., Cramer, A., Bob, K., Calandra, I., Heinz, G., Jöris, O., & Marreiros, J. (2023). Enhancing lithic analysis: Introducing 3d-edgeangle as a semi-automated 3d digital method to systematically quantify stone tool edge angle and design. *Plos one*, 18(11), e0295081.
- Siebert, M., Adelman, J., & Git, Y. (2023). *numpy-append-array*. Github.
- Spyrou, A., Nobles, G., Hadjikoimis, A., Evin, A., Hulme-Beaman, A., Çakırlar, C., ... others (2022). Digital zooarchaeology: State of the art, challenges, prospects and synergies. *Journal of Archaeological Science: Reports*, 45, 103588.
- Wyatt-Spratt, S. (2022). After the revolution: a review of 3d modelling as a tool for stone artefact analysis. *Journal of Computer Applications in Archaeology*.
- Yezzi-Woodley, K., Calder, J., Olver, P. J., Cody, P., Huffstutler, T., Terwilliger, A., ... Tostevin, G. (2021). The virtual goniometer: demonstrating a new method for measuring angles on archaeological materials using fragmentary bone. *Archaeological and Anthropological Sciences*, 13(7), 106.
- Yezzi-Woodley, K., Calder, J., Sweno, M., Siewert, C., & Olver, P. J. (2022). The batch artifact scanning protocol: A new method using computed tomography (ct) to rapidly create three-dimensional models of objects from large collections en masse. *arXiv preprint arXiv:2205.02691*.
- Yezzi-Woodley, K., Terwilliger, A., Li, J., Chen, E., Tappen, M., Calder, J., & Olver, P. (2024). Using machine learning on new feature sets extracted from three-dimensional models of broken animal bones to classify fragments according to break agent. *Journal of Human Evolution*, 187, 103495.

Supplemental Information

7 Sample In Detail

This table shows the full list of sample identifiers, the dimensions of the fragments (in mm), and their volumes ($(mm)^3$) to give a detailed view of the size of the objects and to inform future reproducibility. Though some may be interested in knowing species and skeletal part of these fragments, that is not the focus of this study; such information will be made available when the models are shared.

Table 2: List of Specimens

Specimen	Length	Width	Depth	Volume	Specimen	Length	Width	Depth	Volume
MN19061107	16.261	3.206	1.764	22.982	MN18060315	18.781	14.931	5.054	315.036
MN19061005	33.583	8.507	7.506	495.958	MN19065313	34.161	12.653	4.719	386.377
MN19081508	12.586	3.585	2.117	16.799	MN19063910	27.192	9.441	5.253	218.029
MN18020230	35.495	7.83	3.45	222.423	MN19064914	22.754	10.604	3.436	159.139
MN18021815	12.968	9.771	3.441	125.356	MN19064209	38.388	9.803	4.375	718.229
MN18020117	37.568	21.229	7.235	1754.648	MN18061108	25.128	14.599	9.26	822.62
MN19061112	15.391	9.401	2.273	102.126	MN19063608	16.928	12.261	4.781	296.197
MN19061007	31.533	11.992	4.355	401.301	MN19064913	17.867	9.204	4.087	181.218
MN18020233	31.293	9.197	5.045	352.261	MN19063806	46.475	19.294	9.001	1047.218
MN15011012	11.912	5.265	1.595	26.277	MN19063610	17.631	8.487	3.867	104.51
MN14AA0425	21.113	6.731	4.791	126.232	MN19064507	27.615	11.619	5.329	455.431
MN18020247	31.925	7.722	4.553	301.297	MN19064810	17.014	10.672	3.887	194.981
MN18020611	30.58	12.524	5.357	541.293	MN18060726	21.558	13.357	6.626	347.994
MN15011007	10.472	9.245	4.331	97.593	MN19063908	26.311	11.279	4.261	372.021
MN19081414	20.341	10.173	5.974	356.665	MN18061015	26.629	10.249	5.644	472.464
MN19061808	20.513	8.162	5.505	199.699	MN19063607	20.915	13.491	5.726	400.51
MN18020225	45.039	11.82	6.07	1131.994	MN18061106	33.067	18.887	8.323	931.653
MN18020237	27.659	5.505	4.108	202.07	MN19065308	43.655	18.957	7.245	1302.109
MN19061608	26.06	10.374	4.891	304.988	MN18060722	27.583	17.446	3.913	405.766
MN19062004	27.265	10.247	5.066	460.189	MN18060711	42.527	18.428	8.353	1620.726
MN14AA0522	35.375	9.728	7.498	939.048	MN18061618	17.16	10.385	3.727	129.373
MN18021714	11.994	6.431	2.178	39.066	MN18060806	28.447	8.571	4.962	397.871
MN19061215	16.503	6.571	4.097	100.554	MN18060713	32.117	21.727	9.852	1103.509
MN19062111	12.523	5.373	2.192	37.342	MN18061311	29.356	19.383	5.181	563.452
MN15AA2409	20.623	19.309	6.395	350.8	MN19064004	29.711	8.811	4.63	278.006
MN15010407	28.813	7.857	5.256	277.444	MN19064302	49.661	20.91	9.327	1584.615
MN19062015	37.126	11.965	6.494	790.476	MN19063604	42.484	19.853	9.821	1502.113
MN15010817	8.697	6.609	2.971	43.946	MN19064212	33.882	16.318	5.152	551.985
MN14AA0429	19.081	6.82	6.198	176.067	MN19065028	20.897	6.026	2.533	46.768
MN19062104	33.226	14.408	9.4	1087.99	MN18060809	31.318	11.611	6.572	531.38
MN19081421	33.272	13.742	9.071	743.457	MN18061508	33.465	13.391	6.273	924.858
MN19081506	13.764	7.072	3.521	88.798	MN18060727	24.529	10.566	5.877	361.817
MN18020112	41.452	14.961	5.517	980.611	MN19065411	19.432	8.117	3.079	155.959
MN15AA2408	23.298	17.271	5.456	439.843	MN18030515	26.036	13.225	5.989	563.475
MN19060908	1.58	1.26	0.408	0.304	MN18030514	31.014	9.873	6.477	502.428
MN14AA0322	24.941	9.416	7.014	484.558	MN18080116	21.244	10.034	3.801	235.115
MN19060804	48.347	16.464	6.766	1315.805	MN19081218	20.304	12.126	6.212	548.744
MN19060903	33.071	15.017	8.543	1424.733	MN18080112	48.339	18.5	7.149	1672.388
MN18020109	37.319	20.432	5.864	1236.54	MN19081128	12.887	11.958	5.222	200.322
MN18020833	38.013	12.582	7.609	724.074	MN18030519	29.37	11.827	4.025	287.651
MN19060103	20.133	8.972	5.022	217.291	MN19065105	31.817	20.807	8.045	1129.848
MN14AA0326	26.426	7.368	5.261	210.023	MN19050626	24.604	8.022	7.651	436.281

Table 2 – continued from previous page

Specimen	Length	Width	Depth	Volume	Specimen	Length	Width	Depth	Volume
MN19062304	11.741	8.965	4.555	82.762	MN18030516	27.509	22.368	8.826	355.784
MN19061108	0.994	0.538	0.318	0.066	MN18080117	6.024	2.308	0.483	0.887
MN15010815	14.146	5.009	3.035	56.532	MN18030713	20.973	14.157	5.682	299.842
MN18020246	21.399	9.53	2.894	113.912	MN19050622	2.635	0.765	0.69	0.161
MN18020116	14.37	8.006	2.461	92.789	MN18080113	38.07	16.02	6.206	907.944
MN19081313	24.306	6.371	3.812	147.982	MN18030309	37.013	16.992	11.046	847.642
MN15AA2407	25.207	12.257	4.218	250.189	MN18030814	32.886	13.347	5.806	375.956
MN18020721	18.144	7.632	5.103	221.55	MN18030612	24.623	10.09	7.455	230.288
MN14AA0526	25.115	11.495	6.521	508.459	MN19081207	31.902	13.486	6.391	801.909
MN18020244	28.744	8.158	5.1	320.886	MN18030815	20.026	12.946	5.671	388.576
MN19060911	29.725	10.422	5.927	465.167	MN19065410	30.647	10.88	4.817	626.048
MN13AA0710	67.835	15.016	7.685	2819.52	MN18030813	19.709	16.899	9.121	641.864
MN13AA0810	19.859	11.215	2.818	162.196	MN18030310	38.344	12.633	7.892	813.195
MN18020232	49.616	17.124	9.608	1494.086	MN18030715	24.962	11.251	8.023	475.287
MN19060907	33.35	16.616	5.704	1062.67	MN19050628	2.635	0.765	0.69	0.161
MN19061209	7.868	1.853	1.151	0.631	MN18030809	37.311	15.991	9.243	1412.479
MN13AA0718	25.656	6.815	1.795	46.307	MN18030211	13.747	13.255	6.128	310.141
MN14AA0524	13.991	10.156	3.249	94.455	MN18030210	29.915	12.896	7.54	909.533
MN19061211	18.879	8.469	4.554	270.151	MN19065205	14.723	10.437	2.9	123.811
MN18020248	21.739	13.321	6.403	477.318	MN18030609	25.395	21.428	8.426	1298.089
MN19061217	21.953	7.22	3.374	157.025	MN19081217	21.034	10.746	4.904	351.232
MN19062405	49.035	14.023	7.449	1401.173	MN19050632	17.915	7.702	3.535	131.967
MN19060912	39.104	6.767	4.822	423.019	MN19064605	43.112	19.624	9.906	1505.847
MN19061409	17.864	8.862	3.753	127.95	MN19080704	18.351	9.891	4.02	229.443
MN19062012	10.563	6.646	3.717	89.239	MN18030712	18.339	14.444	7.495	600.775
MN19061113	33.306	10.278	3.507	286.74	MN18030816	17.896	12.597	5.741	190.111
MN19061811	17.838	7.695	2.4	60.994	MN19065108	21.401	9.873	4.293	258.51
MN18020827	29.492	12.132	7.723	824.327	MN19064215	18.701	6.956	3.594	131.828
MN13AA0711	42.549	20.22	10.019	2024.682	MN19064412	18.924	5.894	2.629	57.488
MN19081318	0.533	0.463	0.186	0.011	MN19063810	21.791	7.623	4.531	214.416
MN18021713	26.531	12.796	5.296	374.131	MN19050631	15.071	9.16	6.094	239.543
MN19061216	10.574	10.422	5.066	172.588	MN19081210	37.812	10.217	5.805	628.084
MN18020234	23.967	6.28	3.16	116.21	MN18030714	24.153	16.91	7.884	440.124
MN13AA0716	40.763	14.013	7.058	938.559	MN18030719	15.305	12.709	5.214	291.178
MN18020822	25.91	9.683	3.94	299.494	MN18030110	29.208	7.474	5.444	433.322
MN15AA2504	33.721	16.899	7.357	903.235	MN19064410	14.169	8.034	6.355	137.675
MN19062403	44.041	13.276	5.833	916.31	MN18030414	30.18	20.043	8.21	1319.292
MN19062109	57.792	8.323	5.482	666.036	MN18080114	44.84	12.907	7.652	873.739
MN19062009	16.834	11.637	4.506	175.982	MN19065409	36.32	12.484	5.78	387.324
MN18020830	45.834	9.985	5.239	555.174	MN18030906	39.714	23.4	11.698	2881.996
MN15010611	23.917	6.994	2.098	88.231	MN19081110	36.513	10.998	4.266	435.64
MN19060505	38.065	10.191	8.392	1279.269	MN18030418	33.635	10.773	7.915	440.166
MN14AA0323	13.601	9.281	2.226	70.052	MN18080110	44.343	19.192	7.68	1557.382

Table 2 – continued from previous page

Specimen	Length	Width	Depth	Volume	Specimen	Length	Width	Depth	Volume
MN19060803	20.329	13.325	8.709	140.966	MN19081222	23.592	12.513	7.187	315.008
MN15AA2410	16.612	6.787	2.18	71.873	MN18030711	25.433	13.076	7.394	556.284
MN18020720	19.078	7.49	4.219	257.64	MN18030717	17.477	14.293	4.607	381.812
MN19081413	44.035	14.263	6.404	1352.274	MN19050627	20.105	5.776	3.032	111.248
MN19060705	36.433	15.667	6.667	973.011	MN19081204	46.111	20.523	9.069	1425.81
MN19062406	30.508	11.922	4.862	630.763	MN18030108	24.16	13.81	5.618	477.135
MN19060205	62.579	20.444	11.671	2646.75	MN19081211	39.681	15.795	8.932	540.726
MN13AA0709	34.649	23.773	8.913	1434.955	MN19081212	37.684	8.022	4.969	393.092
MN19081412	31.164	16.931	10.824	697.314	MN18030311	35.402	9.666	6.137	519.775
MN19062014	26.531	6.502	3.515	181.072	MN19081114	28.787	14.97	5.565	450.886
MN19062006	26.475	9.508	4.049	176.468	MN19080703	20.809	15.658	7.385	479.127
MN19061412	36.71	7.762	3.761	214.094	MN18030716	23.688	12.939	5.962	380.759
MN19061610	18.182	10.178	6.042	368.464	MN18030610	24.726	14.579	9.256	538.126
MN19061414	16.526	5.497	4.347	92.235	MN18030720	21.613	10.458	5.584	324.789
MN19061114	26.947	9.186	4.706	256.765	MN19064216	18.85	4.841	3.516	105.576
MN19061605	27.288	9.954	3.396	171.565	MN18030109	27.743	8.788	5.351	233.305
MN18020609	10.438	9.627	4.647	102.883	MN19081221	22.422	11.625	8.356	512.424
MN19062005	68.259	16.825	9.604	2068.275	MN18080118	17.852	8.846	4.866	184.223
MN19081317	1.963	0.671	0.307	0.14	MN19081216	19.536	9.932	8.804	376.565
MN19061810	14.351	6.22	3.224	67.228	MN19050634	18.989	5.787	2.99	54.152
MN19062011	15.359	9.412	3.327	74.362	MN18030611	23.373	12.007	4.294	328.112
MN19061214	16.189	3.552	1.314	15.133	MN19065018	14.09	11.286	5.945	192.577
MN19062105	47.354	15.028	6.3	1368.341	MN18080111	46.622	20.319	10.816	2089.552
MN19061410	24.815	8.793	3.513	158.715	MN18030518	27.496	10.739	5.628	425.489
MN19081310	25.414	10.359	4.635	177.646	MN18030718	19.006	11.716	5.545	444.963
MN19061106	48.821	9.064	8.477	767.485	MN18030723	13.574	9.861	2.921	104.945
MN18020221	55.395	16.627	5.537	1649.318	MN19081209	42.328	12.259	8.203	1606.17
MN15010816	19.777	6.68	6.392	151.09	MN18030721	19.768	11.499	3.595	165.214
MN14AA0435	20.528	8.107	2.327	119.628	MN18030708	43.507	20.221	9.622	2580.686
MN19081418	38.946	12.978	7.337	932.435	MN18030413	39.538	19.192	10.504	2045.997
MN19081415	30.561	15.882	5.284	577.526	MN19081205	49.143	13.53	7.479	1644.434
MN18020250	25.509	9.498	6.081	441.916	MN19050635	14.611	6.898	5.481	200.984
MN13AA0812	26.627	9.92	3.681	279.198	MN19064606	34.545	13.037	7.741	675.152
MN19081505	21.932	11.632	5.583	209.385	MN190812119	23.241	10.722	4.8	411.485
MN18020820	30.348	12.515	7.028	724.466	MN18080115	24.878	10.813	4.352	353.45
MN19061210	46.461	11.188	5.239	799.867	MN18030811	26.831	18.29	4.881	470.813
MN18020920	23.08	3.762	1.42	23.057	MN19081223	24.88	10.203	3.801	358.868
MN15011005	18.27	8.668	2.668	101.966	MN18030613	22.586	8.202	6.931	370.504
MN18021812	18.23	6.296	2.445	78.772	MN19081213	35.905	9.593	6.421	513.989
MN18020908	18.874	13.163	5.02	387.465	MN19081215	24.436	13.652	6.746	534.806
MN19081315	12.177	8.285	3.03	80.313	MN18030923	15.008	8.527	3.138	124.123
MN18020831	21.455	10.238	6.433	277.686	MN18030722	15.14	9.078	5.084	151.642
MN19060808	23.09	8.079	3.73	176.829	MN19081220	23.299	15.005	1.998	166.401

Table 2 – continued from previous page

Specimen	Length	Width	Depth	Volume	Specimen	Length	Width	Depth	Volume
MN18020110	36.618	22.173	8.765	2008.994	MN18030608	33.553	13.803	7.509	1345.535
MN15AA2507	13.329	8.722	3.594	84.123	MN19065107	32.929	13.85	8.486	601.666
MN13AA0723	35.307	15.173	5.607	542.907	MN18030308	52.183	18.095	9.998	1480.021
MN18021306	0.183	0.162	0.107	0.001	MN19063809	19.758	8.422	3.002	136.917
MN18020242	35.553	12.052	7.709	585.236	MN19064411	17.564	6.473	3.312	88.6
MN19060504	23.046	12.572	7.289	784.541	MN18030709	32.578	18.4	8.537	1208.685
MN19061807	40.055	9.639	5.222	303.131	MN18090211	47.604	13.637	5.94	1140.891
MN18020238	11.761	5.417	1.412	24.463	MN18080711	36.904	10.531	4.274	526.459
MN18020231	21.66	10.253	3.88	290.393	MN18080512	22.507	18.519	5.343	591.776
MN19061105	22.472	6.98	2.271	58.745	MN19081037	27.028	6.663	5.182	307.176
MN13AA0726	39.073	25.488	9.231	1781.94	MN19080938	31.287	18.792	9.773	1659.02
MN19062110	62.387	11.857	7.809	1808.065	MN19050612	38.54	17.61	6.583	1977.726
MN19061809	12.469	8.208	3.998	139.255	MN19050244	37.837	14.521	9.547	1937.579
MN18020245	20.137	9.254	4.267	168.343	MN18080617	21.173	12.891	4.611	361.898
MN18020227	41.478	14.102	5.755	939.9	MN19050259	19.165	8.558	4.963	211.095
MN18020220	63.339	15.059	6.896	1738.604	MN19080939	37.464	11.43	4.256	721.728
MN13AA0917	18.008	9.373	4.425	118.321	MN19081027	29.99	8.028	5.492	407.894
MN13AA0724	38.795	12.012	7.564	1226.391	MN18080416	45.097	20.43	7.681	1429.7
MN14AA0324	42.238	12.773	6.364	721.924	MN18080417	54.221	16.815	7.964	1931.941
MN19061207	33.825	14.275	3.726	335.618	MN18080513	26.19	15.136	6.304	596.272
MN19081316	14.579	3.416	1.14	13.583	MN18080621	17.367	8.321	4.331	154.931
MN18020829	39.51	10.712	3.652	333.821	MN19050254	24.229	14.543	6.623	532.292
MN19081410	28.315	11.805	4.523	324.706	MN18090807	49.431	12.12	6.217	958.14
MN18021814	10.892	5.928	2.656	40.393	MN11AA0504	34.889	13.485	8.504	779.056
MN14AA0521	45.672	10.476	5.329	671.033	MN19050630	15.635	12.828	5.276	189.964
MN19061413	14.142	11.028	4.346	139.584	MN19050245	35.107	14.865	7.167	1059.496
MN13AA1025	19.72	10.227	3.733	139.029	MN19050623	27.325	14.594	3.962	225.882
MN18020118	11.53	10.426	4.59	189.233	MN18090216	25.937	12.378	6.918	736.193
MN15010814	27.851	7.245	4.748	235.933	MN18080423	34.741	12.389	6.439	786.324
MN19062010	45.387	6.079	3.358	203.455	MN18080432	19.792	10.008	6.332	342.151
MN19081319	8.44	1.895	1.238	4.412	MN18080428	25.234	10.272	4.536	288.947
MN19061609	23.042	12.994	8.034	493.595	MN19050258	36.306	7.585	4.907	607.243
MN18020911	12.224	8.756	3.931	125.804	MN19050611	41.131	19.054	7.883	1641.557
MN18020723	12.2	1.07	0.81	1.314	MN19050610	42.315	18.504	5.193	1273.059
MN19060910	25.186	10.538	7.965	582.433	MN19050811	34.848	12.091	6.149	728.147
Mn19062103	45.089	13.989	8.305	875.368	MN18090309	50.855	14.885	7.463	1761.297
MN19060909	54.666	15.469	11.994	1426.552	MN19050545	35.871	13.229	6.421	991.649
MN19081503	36.543	10.018	4.412	333.272	MN18090214	41.401	15.351	6.836	1463.304
MN19061408	35.844	8.392	6.307	778.512	MN18080616	25.898	12.378	5.844	464.639
Mn18021305	8.414	4.196	1.004	7.166	MN19081020	34.748	12.694	6.298	1089.365
MN13AA0712	35.658	14.8	6.938	976.959	MN19050621	30.306	9.428	5.413	403.776
MN18020229	41.548	19.802	9.934	2242.375	MN19080936	37.382	12.082	6.57	937.655
MN19062112	39.984	8.63	2.903	203.945	MN19050552	30.904	11.685	7.84	759.291

Table 2 – continued from previous page

Specimen	Length	Width	Depth	Volume	Specimen	Length	Width	Depth	Volume
MN19081419	24.671	10.602	5.043	450.023	MN19050813	32.47	10.917	7.195	456.06
MN18020228	9.255	5.84	1.614	4.988	MN18080510	51.77	16.309	7.307	1280.794
MN19062013	24.542	8.146	4.4	223.176	MN19050636	12.371	9.32	4.396	117.798
MN13AA0720	38.233	16.918	8.864	1409.231	MN19050124	36.573	8.709	7.182	868.322
MN19060905	30.848	15.098	6.302	671.644	MN11AA0505	38.803	10.362	7.84	780.19
MN15AA2411	26.126	12.055	4.42	193.424	MN19081021	33.217	14.731	7.207	1106.181
MN19060404	36.941	10.173	6.111	617.047	MN19050608	40.601	19.887	8.254	1806.61
MN19062107	48.044	21.177	10.765	2492.061	MN18080435	19.908	5.809	3.43	89.452
MN13AA0813	44.567	10.944	6.183	945.027	MN19080940	35.491	13.645	5.099	652.735
MN15010509	26.752	7.017	2.943	138.203	MN19050617	25.69	14.515	5.443	585.006
MN18020722	37.894	7.15	5.039	395.341	MN19050540	36.779	17.163	6.987	1340.472
MN19061115	45.712	8.982	4.179	405.708	MN18080434	16.926	8.866	3.814	137.547
MN19061213	3.23	1.926	0.62	0.593	MN19050551	31.291	13.7	10.294	970.181
MN19081420	27.27	11.951	5.993	465.184	MN11AA0807	32.089	10.726	4.495	266.925
MN19062008	17.856	9.969	4.69	261.487	MN19081023	32.768	11.597	6.286	730.524
MN14AA0327	60.322	12.941	5.535	665.252	MN19050262	22.819	9.587	3.425	146.15
MN19062407	28.798	9.886	2.865	245.424	MN18080419	50.061	17.439	9.442	2069.184
MN18020719	20.456	7.886	4.966	324.411	MN19081026	34.405	11.377	7.247	597.484
MN19061006	40.253	10.201	3.658	507.145	MN19050607	25.283	5.729	2.213	18.5
MN13AA0715	23.081	6.415	2.23	44.973	MN18080424	43.931	12.058	5.383	1024.238
MN19081320	17.705	7.117	5.242	141.754	MN18080511	34.948	19.203	7.247	1023.059
MN19060706	13.367	9.793	4.637	144.179	MN19080845	29.588	13.378	6.145	886.963
MN13AA0717	25.684	10.162	4.635	246.458	MN18080620	15.508	8.802	4.146	209.213
MN19060906	57.623	18.657	10.309	2374.089	MN19050624	21.246	14.312	4.924	313.469
MN18020111	50.28	18.706	7.477	1365.192	MN18090106	34.485	19.419	9.047	1174.43
MN18020922	21.323	8.338	4.765	176.249	MN19050620	28.074	7.7	5.343	390.702
MN19061411	30.276	9.927	5.125	598.296	MN19050629	18.659	10.688	4.315	264.399
MN19061109	0.142	0.085	0.057	0	MN18080436	12.781	6.02	4.186	79.845
MN19061004	33.186	17.832	7.414	1188.384	MN19081025	36.267	9.491	4.903	731.625
MN19081309	14.668	7.388	3.742	59.017	MN18080433	17.793	7.717	5.344	186.449
MN18020240	52.456	13.402	7.069	1019.448	MN19081038	24.512	10.492	3.692	262.486
MN18020239	32.235	11.108	7.179	762.525	MN11AA0411	44.271	8.917	4.934	461.43
MN19061003	33.382	14.339	7.288	938.256	MN11AA0705	51.143	13.344	9.457	1965.39
MN13AA0722	35.505	14.176	7.586	1049.145	MN19081024	32.979	11.28	7.306	976.593
MN19081411	30.123	2.812	1.155	10.758	MN18080431	25.551	8.027	3.668	211.045
MN18020243	33.703	21.962	7.594	1445.019	MN19050625	15.925	12.077	5.467	275.533
MN19061218	18.679	11.417	4.504	215.092	MN18080514	28.328	13.492	5.224	454.163
MN13AA0721	27.296	18.03	6.287	629.836	MN18090213	33.868	10.053	5.295	431.905
MN14AA0410	24.901	8.993	6.548	282.316	MN18080704	44.191	14.902	10.113	1667.504
MN18020921	11.665	9.506	3.908	116.52	MN19080942	32.655	8.167	5.932	415.33
MN19081507	13.928	10.055	5.423	202.165	MN19080844	28.938	12.171	10.558	1079.39
MN14AA0329	25.972	7.569	4.376	172.901	MN19080941	33.606	16.216	6.372	775.18
MN14AA0423	18.873	7.243	3.917	161.762	MN19050616	26.451	16.825	7.907	945.926

Table 2 – continued from previous page

Specimen	Length	Width	Depth	Volume	Specimen	Length	Width	Depth	Volume
MN19062007	20.914	9.536	4.105	298.867	MN19081030	28.22	12.528	6.4	781.137
MN19062106	36.08	19.239	7.597	1223.51	MN19081031	23.172	11.036	6.437	555.471
MN19081504	26.76	5.437	2.195	67.471	MN11AA0608	34.768	12.586	9.094	812.88
MN18020241	47.517	6.657	4.123	299.636	MN18090310	29.048	8.222	4.863	290.49
MN18020832	21.785	10.128	6.752	336.407	MN19080937	33.887	11.812	6.422	827.455
MN19061606	32.946	9.77	7.468	644.028	MN19050609	35.304	17.295	8.763	1729.259
MN19061110	0.141	0.081	0.055	0	MN11AA0412	35.1	9.14	5.914	556.713
MN14AA0320	14.382	7.193	1.626	54.439	MN19081028	28.618	16.962	5.758	700.576
MN19062108	32.202	7.736	2.718	145.688	MN18080619	20.882	10.303	4.079	370.864
MN19062003	54.835	20.097	10.872	2985.124	MN19050255	26.238	11.429	5.714	435.136
MN10AA1004	59.735	20.639	11.01	5061.162	MN18080427	29.055	8.141	6.581	446.215
MN12AA1108	66.208	20.054	6.827	3301.157	MN19050550	37.557	12.243	6.998	987.42
MN12AA5604	68.444	21.544	9.315	3394.424	MN19050257	30.313	9.166	5.015	236.542
MN12AA0507	66.159	18.469	9.616	3106.812	MN19050618	23.161	15.865	5.591	442.498
MN12AA6116	57.33	6.208	4.645	443.257	MN19081036	23.142	9.553	3.052	159.369
MN19061206	59.094	21.299	10.085	2683.975	MN19050613	33.491	14.954	6.42	758.073
MN13AA0211	55.55	20.641	9.802	2718.608	MN19081009	34.888	15.51	5.804	523.496
MN13AA0313	54.799	17.889	6.391	1364.069	MN18090107	27.338	11.207	7.035	380.821
MN12AA1109	69.387	16.723	7.528	2305.565	MN18080214	26.646	13.734	5.628	638.114
MN12AA6608	72.569	14.787	6.808	1471.802	MN19050619	36.797	8.421	5.579	457.008
MN12AA6606	71.562	22.032	8.714	4085.483	MN18080420	28.982	20.504	8.696	990.355
MN12AA6407	46.971	19.871	4.628	895.103	MN19081034	24.033	8.478	7.756	591.18
MN12AA0207	55.286	22.124	7.779	3689.891	MN18080516	33.106	10.989	4.896	416.5
MN12AA0302	54.831	14.857	7.997	2170.832	MN18080421	40.119	14.405	5.413	1095.46
MN10AA0905	60.143	14.233	9.732	2619.489	MN19050534	36.595	15.216	14.606	2129.891
MN12AA6615	57.713	9.075	4.189	571.043	MN19050615	25.779	23.646	6.498	998.443
MN13AA0111	58.131	21.147	7.27	2935.424	MN19050814	8.854	2.836	2.308	3.234
MN12AA6110	52.977	12.69	9.46	1751.417	MN18080307	32.13	13.945	5.266	731.099
MN12AA1110	48.533	23.757	7.328	2032.176	MN19050809	33.292	17.415	8.137	1479.269
MN19061304	64.942	15.408	10.851	2820.604	MN19080823	47.622	13.098	6.432	808.955
MN12AA6610	42.13	18.226	4.644	1321.262	MN13AA0619	27.452	9.077	4.381	246.93
MN10AA0706	67.862	13.386	8.656	2807.132	MN13AA1123	26.393	12.486	8.43	1117.144
MN19061305	66.285	10.394	6.318	1093.082	MN19080923	60.42	15.523	6.674	2663.055
MN12AA6409	44.779	12.743	7.379	827.519	MN11AA0811	32.465	15.916	8.197	979.829
MN12AA6514	35.113	7.51	4.079	249.18	MN19080604	24.115	7.659	2.546	219.42
MN12AA6008	54.224	18.043	8.058	2620.859	MN19050409	26.359	12.614	5.48	418.385
MN12AA6509	58.648	20.111	8.193	1439.709	MN13AA1217	25.887	12.83	4.257	340.898
MN12AA6013	54.739	5.745	3.838	320.419	MN13AA0617	23.019	8.935	3.214	154.797
MN12AA6009	58.584	20.075	7.055	2045.758	MN19065024	12.707	6.633	3.338	101.96
MN10AA0107	40.241	11.512	5.123	656.894	MN19080817	38.58	18.276	9.806	1968.672
MN12AA0410	36.196	12.744	5.768	733.911	MN13AA1121	27.062	11.023	8.133	879.04
MN12AA6216	22.737	6.058	4.528	196.592	MN19063704	62.835	17.361	4.625	1576.142
MN12AA1113	33.938	22.327	7.001	1398.961	MN19081018	49.064	10.066	8.142	1854.567

Table 2 – continued from previous page

Specimen	Length	Width	Depth	Volume	Specimen	Length	Width	Depth	Volume
MN10AA0207	40.1	19.093	10.227	2723.421	MN13AA1029	32.432	15.012	9.038	1259.924
MN19063005	36.298	15.357	8.397	1035.367	MN18080213	34.417	12.605	6.601	360.938
MN19060605	42.796	19.181	8.208	1586.893	MN18060709	61.878	20.239	9.54	3802.655
MN19063007	25.101	9.653	3.634	236.443	MN13AA1031	25.937	15.264	10.158	858.743
MN12AA6017	38.611	18.249	7.469	1294.809	MN13AA0510	24.024	14.951	6.173	297.221
MN12AA6018	35.098	12.745	3.189	280.678	MN19081206	59.062	11.836	7.177	2119.4
MN12AA0216	34.722	13.109	7.545	915.844	MN13AA1128	31.261	10.256	4.657	241.651
MN13AA0116	24.878	18.783	10.039	1410.735	MN13AA0513	32.444	12.5	8.385	738.11
MN10AA0809	33.596	20.283	8.922	1561.87	MN19064812	14.099	7.196	2.777	70.033
MN10AA1005	50.108	19.116	8.982	3915.446	MN19065009	53.19	17.549	8.918	2109.207
MN10AA1006	47.196	8.179	5.952	920.165	MN19080843	42.045	11.283	6.487	962.047
MN10AA0908	47.234	15.839	9.364	1957.713	MN19063904	60.386	13.324	7.811	2091.972
MN12AA6105	44.488	13.327	6.291	533.381	MN13AA1219	30.164	13.781	5.034	714.214
MN10AA0607	43.535	13.435	10.406	2156.594	MN13AA1120	30.851	16.671	6.352	880.583
MN12AA0209	33.549	21.482	8.075	1336.389	MN19063811	19.578	7.974	4.068	156.862
MN19063107	40.833	13.689	5.146	888.362	MN19080846	41.447	10.449	4.507	479.173
MN10AA0910	38.113	14.631	6.887	917.613	MN13AA0816	17.826	11.492	5.382	252.195
MN10AA0108	38.932	10.601	5.031	395.335	MN13AA0512	28.937	16.853	13.642	0
MN12AA6517	41.014	8.187	3.798	254.742	MN11AA0606	42.68	19.258	10.744	2880.474
MN12AA6618	33.962	13.133	5.441	671.721	MN19065109	22.344	9.818	4.415	222.023
MN13AA0216	35.687	12.417	4.952	673.818	MN18080612	34.752	6.875	5.19	358.124
MN12AA0807	41.104	23.98	9.642	2075.364	MN19063603	56.47	21.481	10.175	2392.427
MN12AA0511	43.131	19.312	5.387	1563.412	MN19064207	67.612	12.722	5.323	1165.208
MN12AA6109	36.216	14.662	6.32	874.553	MN13AA1125	28.859	14.307	7.711	807.769
MN10AA1011	36.949	14.005	7.074	1358.555	MN19064506	46.997	6.976	5.553	503.879
MN12AA0509	45.745	20.123	9.576	2323.268	MN13AA0512	24.259	11.91	6.738	380.657
MN19062906	42.3	17.307	9.24	1315.898	MN13AA1220	33.371	8.141	6.337	553.031
MN19062904	43.857	19.096	10.218	1423.917	MN19080842	39.973	8.682	5.31	764.447
MN12AA0512	47.651	20.296	8.525	2495.179	MN13AA1028	37.046	14.815	7.421	1015.085
MN10AA0710	44.462	11.699	7.424	1423.768	MN18080208	50.192	23.19	6.362	2356.042
MN13AA0215	31.72	12.084	5.173	463.429	MN19064505	54.459	10.868	7.541	1050.31
MN12AA0808	35.456	21.489	9.414	1998.097	MN19080826	45.236	9.787	8.778	1224.136
MN19061306	49.822	16.638	8.274	1708.451	MN13AA1124	27.347	9.223	8.064	654.263
MN12AA6106	34.519	14.683	7.382	1163.212	MN11AA0810	42.707	12.176	10.966	1067.109
MN12AA1115	28.029	11.223	8.48	278.614	MN18090808	42.655	11.15	5.599	785.776
MN13AA0319	37.958	8.834	3.421	144.521	MN13AA0416	27.368	16.552	6.281	411.313
MN10AA1007	41.684	17.961	11.133	2429.325	MN18080211	36.113	15.688	9.878	1666.108
MN12AA6217	34.724	10.899	3.854	301.816	MN13AA1032	23.405	11.377	7.061	511.57
MN10AA2011	31.644	13.958	4.86	384.59	MN19080921	67.552	14.654	7.591	1710.053
MN10AA0105	44.467	21.58	11.008	2043.746	MN19064805	52.934	10.377	8.714	914.166
MN10AA0405	39.026	10.257	6.449	502.454	MN19064404	49.521	15.939	6.668	1578.493
MN12AA6611	43.133	16.111	3.956	620.082	MN13AA1216	29.557	12.123	5.879	462.043
MN13AA0332	38.255	9.355	5.08	585.84	MN19065307	59.303	13.026	9.329	1546.183

Table 2 – continued from previous page

Specimen	Length	Width	Depth	Volume	Specimen	Length	Width	Depth	Volume
MN13AA0115	31.75	12.145	3.174	281.984	MN13AA1035	29.822	13.501	4.991	320.262
MN10AA0413	39.673	12.068	8.334	1262.645	MN19080821	42.935	15.82	10.044	1557.215
MN19061803	50.291	19.803	10.688	2879.58	MN13AA0415	34.607	10.664	4.391	759.873
MN13AA0118	30.179	18.851	9.244	1168.022	MN19063906	55.285	14.376	6.768	1658.351
MN12AA6617	28.748	12.237	8.585	771.132	MN13AA0915	29.572	14.459	5.079	446.584
MN12AA0704	44.211	20.205	11.262	1875.316	MN19065306	57.19	13.937	7.042	1571.402
MN10AA2009	39.732	16.004	4.64	663.941	MN18090809	36.611	15.302	4.737	655.121
MN10AA1804	33.74	11.091	7.334	445.333	MN19081109	53.206	14.573	9.45	2231.016
MN12AA6515	46.119	6.875	3.539	288.499	MN19080924	64.569	13.849	7.417	1862.921
MN13AA0316	40.465	8.046	3.877	290.629	MN18080610	54.987	15.448	5.854	1571.44
MN12AA6616	36.285	10.899	7.104	766.716	MN19065103	62.739	21.28	12.384	2391.944
MN13AA0114	34.648	13.111	6.344	511.027	MN11AA0809	35.191	11.56	6.221	668.531
MN12AA0910	32.108	18.726	8.659	1915.574	MN19080702	60.791	17.717	9.785	2032.692
MN10AA0106	43.611	9.634	7.282	815.479	MN18090810	53.229	9.758	3.72	668.757
MN10AA0509	36.12	10.841	6.062	559.09	MN18090806	53.582	14.441	8.085	1471.215
MN19061308	37.571	9.511	5.05	408.633	MN13AA0615	33.276	11.476	4.187	462.903
MN12AA6609	40.213	15.769	3.767	871.166	MN19065304	66.907	22.691	11.046	4026.085
MN10AA0909	43.055	13.769	5.574	953.39	MN13AA0420	30.111	7.699	2.53	171.469
MN10AA0109	37.045	8.859	5.578	462.208	MN13AA1116	24.934	14.391	5.681	483.843
MN12AA6218	21.934	7.782	3.135	113.533	MN19080814	54.076	13.662	12.238	2559.666
MN12AA6016	36.908	21.159	5.932	767.717	MN19080910	69.044	12.325	10.844	2566.378
MN12AA5605	44.729	15.242	10.88	883.904	MN19080819	33.047	16.154	9.297	1423.056
MN12AA0217	40.992	14.714	7.983	1502.796	MN18080212	47.329	8.949	6.183	911.295
MN12AA6613	39.163	15.798	3.797	571.373	MN13AA1030	30.791	10.754	5.486	224.226
MN19060609	35.101	13.607	5.164	454.942	MN19080822	42.142	15.278	8.801	1804.36
MN12AA6112	49.95	10.51	7.246	715.535	MN19080815	51.681	12.646	7.221	1663.942
MN12AA0912	46.437	22.876	10.611	4140.496	MN18080615	31.425	10.843	5.28	519.72
MN12AA5620	34.309	11.761	6.916	516.811	MN13AA0418	21.554	9.333	3.867	174.393
MN12AA6512	30.907	12.662	5.328	821.973	MN13AA0814	22.436	11.923	4.8	304.368
MN12AA6612	41.802	10.14	5.641	477.437	MN13AA1027	30.05	15.804	6.446	765.957
MN12AA6011	35.746	20.282	7.8	1726.47	MN19064811	18.743	7.37	3.143	103.296
MN19061104	46.623	22.027	11.044	2372.247	MN19063813	21.974	5.74	3.214	110.387
MN12AA0305	29.686	10.947	2.65	327.859	MN19080841	27.939	14.551	8.774	950.484
MN12AA0705	40.76	9.235	4.666	578.636	MN18080613	30.225	9.527	6.148	544.423
MN13AA0119	35.812	17.057	10.135	1504.942	MN19065011	48.905	22.754	5.647	1506.764
MN19063006	46.25	15.726	5.378	785.572	MN19080847	30.824	11.108	5.656	556.458
MN10AA0708	51.436	19.831	8.694	2477.636	MN18080210	52.086	15.787	8.403	1764.719
MN19060606	41.755	21.059	8.193	1237.197	MN19063812	20.766	7.244	4.452	183.763
MN12AA6113a	32.637	18.817	6.509	1019.624	MN13AA1114	29.736	6.151	5.83	372.759
MN12AA6107	28.485	12.424	6.489	574.531	MN19080603	22.073	7.545	7.253	407.524
MN10AA0808	23.741	12.04	9.092	758.698	MN19081208	59.584	15.866	10.251	2963.049
MN19061806	24.534	13.884	6.687	468.725	MN18090707	42.886	12.174	4.067	617.234
MN10AA0408a	27.367	13.745	7.172	571.909	MN19063804	59.465	18.072	9.542	2592.018

Table 2 – continued from previous page

Specimen	Length	Width	Depth	Volume	Specimen	Length	Width	Depth	Volume
MN12AA0119	25.729	15.443	4.143	373.077	MN13AA1117	28.534	12.414	7.175	839.504
MN10AA0511	21.808	9.817	4.386	258.202	MN19080816	54.122	13.969	8.615	1458.387
MN10AA0407	27.113	14.135	7.261	760.853	MN18032106	19.091	11.639	7.104	457.36
MN10AA0410	18.163	13.843	4.592	352.678	MN18101427	19.109	11.313	4.494	322.843
MN12AA5709	36.188	16.374	5.908	990.712	MN13AA1115	34.934	8.449	3.907	248.932
MN12AA0113	22.426	18.586	5.904	667.84	MN18071719	17.802	9.368	4.066	189.04
MN12AA0118	24.242	13.335	3.687	272.757	MN18071819	35.485	12.97	10.847	1722.623
MN12AA1117	30.304	17.196	5.078	512.674	MN18071119	30.408	18.979	6.224	552.175
MN10AA0912	21.316	12.915	8.547	728.08	MN13AA1020	42.8	20.518	7.308	1866.047
MN12AA6119	22.957	12.292	5.204	261.92	MN18101428	22.17	11.304	3.854	230.212
MN19063113	11.968	9.984	4.195	147.158	MN13AA0511	42.125	15.604	6.471	1067.419
MN19061310	21.822	9.655	5.883	346.939	MN18031226	21.068	14.397	5.115	434.631
MN12AA5710	20.054	16.33	4.777	456.248	MN18030421	21.538	12.006	6.168	478.353
MN19061307	21.703	11.003	5.271	525.883	MN18072336	23.487	16.923	6.399	785.901
MN12AA0122	20.676	14.178	4.463	287.656	MN18032006	35.351	20.697	7.046	1619.985
MN10AA0409	21.009	8.645	6.296	399.812	MN18071418	22.809	15.365	5.144	443.092
MN10AA0110	30.911	11.753	5.176	508.664	MN13AA1022	46.325	18.816	9.592	2751.21
MN10AA0612	30.204	12.634	7.486	633.651	MN18101443	19.884	6.658	4.162	152.039
MN10AA1908	31.732	15.378	5.779	496.682	MN18072335	23.143	15.318	6.028	614.105
MN12AA0111	34.177	20.263	4.277	813.005	MN18072020	34.183	14.066	7.898	1411.458
MN12AA0110	24.072	13.872	5.266	369.822	MN18031920	29.086	13.989	5.485	472.497
MN19063118	16.253	6.982	3.46	93.06	MN18071417	22.55	16.596	7.704	1126.367
MN10AA1014	26.72	17.305	5.642	608.992	MN18101420	32.66	12.074	5.653	520.517
MN12AA0115	28.8	12.049	6.554	660.071	MN18101431	15.73	8.586	5.759	285.463
MN12AA5613	23.414	7.643	4.183	181.467	MN18071620	29.025	16.042	4.582	567.049
MN19063111	30.047	9.09	4.578	308.299	MN18071617	33.503	18.881	3.936	1055.168
MN12AA0920	28.749	15.56	5.735	597.044	MN18101437	15.889	8.294	4.594	210.403
MN19060611	15.325	10.502	4.121	183.049	MN18030420	21.511	11.777	11.092	673.987
MN10AA0913	14.402	11.355	4.518	230.134	MN13AA0616	48.509	12.469	6.315	636.203
MN10AA0408b	30.349	21.573	8.269	1129.123	MN18031218	38.818	13.12	9.203	1266.539
MN19063012	21.381	7.396	5.429	148.893	MN18072334	32.029	14.598	8.243	744.467
MN12AA6518	24.26	10.617	3.82	229.439	MN13AA1122	36.953	17.435	9.047	1163.619
MN19063112	23.73	6.497	4.087	253.036	MN18071717	20.1	8.499	3.695	173.358
MN12AA0916	32.976	24.763	11.629	2487.133	MN13AA1109	49.339	10.615	6.603	441.166
MN12AA5814	30.401	13.405	7.283	827.528	MN18031013	20.982	10.908	5.147	295.373
MN12AA0909	33.629	13.629	7.159	1035.32	MN18031919	28.062	17.572	7.932	779.312
MN19063110	20.191	11.899	4.874	272.153	MN18071822	31.941	14.554	7.423	934.306
MN10AA0111	22.752	8.388	4.874	202.627	MN18072407	31.921	16.754	5.277	705.074
MN10AA0114	22.653	10.385	6.295	312.658	MN18072104	31.727	10.776	5.836	474.079
MN10AA1806	24.022	12.863	4.493	373.913	MN13AA1129	44.949	11.724	6.056	786.116
MN12AA0116	29.504	9.152	4.442	224.653	MN18031114	48.161	5.861	3.277	279.52
MN12AA0112	29.743	15.297	8.597	1674.931	MN18071815	36.899	17.861	7.554	1824.565
MN12AA0121	20.412	15.486	6.324	630.986	MN18031008	24.038	15.688	7.457	976.602

Table 2 – continued from previous page

Specimen	Length	Width	Depth	Volume	Specimen	Length	Width	Depth	Volume
MN12AA0409	27.816	14.497	9.202	984.51	MN18071923	34.001	17.803	7.454	1688.794
MN10AA2008	35.484	14.011	7.93	863.009	MN18101432	25.884	8.319	4.988	196.494
MN19061309	21.719	9.327	6.047	382.195	MN18101424	18.182	14.73	4.629	531.096
MN19063117	16.799	6.83	5.034	155.178	MN18032010	21.295	13.066	8.046	592.477
MN19062404	35.142	14.261	5.78	921.879	MN18071420	26.245	15.015	4.544	245.396
MN12AA6113b	30.241	15.424	4.023	525.572	MN18072716	26.534	11.466	5.234	467.427
MN12AA5815	23.057	15.11	5.894	514.29	MN13AA1021	39.118	24.109	7.19	2288.688
MN12AA0907	34.803	18.388	8.031	1640.972	MN18072323	36.591	17.579	7.644	1237.142
MN12AA0114	26.14	14.651	10.49	940.896	MN18031216	33.945	20.81	6.452	1280.234
MN12AA0214	28.343	12.47	7.323	704.505	MN18072103	33.013	17.147	5.239	681.765
MN10AA0208	32.434	11.464	5.72	498.359	MN18071703	23.92	17.703	10.137	1579.215
MN12AA6014	31.562	17.117	7.028	1108.087	MN18031217	48.374	12.237	7.498	1649.01
MN12AA0921	23.232	14.841	5.744	512.064	MN18032009	31.357	13.362	7.611	1028.809
MN10AA0609	24.735	13.552	10.441	758.496	MN18101423	26.929	13.784	4.911	317.246
MN12AA5810	17.981	13.647	6.007	262.57	MN18031916	30.438	17.479	9.434	1018.327
MN12AA0611	25.212	12.37	5.804	529.503	MN18032111	23.085	8.756	3.603	218.605
MN12AA6516	26.423	13.94	3.326	240.462	MN18101422	28.076	12.585	5.21	539.887
MN12AA6213	24.312	11.557	7.325	685.126	MN18031318	21.33	9.112	3.625	166.746
MN19061805	24.775	15.326	5.652	739.629	MN13AA0912	48.284	14.407	5.818	1184.635
MN10AA0811	31.536	7.14	3.722	330.044	MN18072337	21.832	14.112	6.728	554.618
MN10AA0116	16.645	11.898	5.301	342.241	MN18072331	23.363	18.637	7.392	1000.919
MN19063114	15.522	9.658	4.791	152.827	MN18031313	27.371	14.211	7.112	794.108
MN12AA5618	18.028	6.062	2.404	77.975	MN18071824	29.478	9.224	9.17	701.686
MN10AA0507	15.479	13.283	6.265	398.253	MN18072330	24.661	19.363	6.61	904.083
MN10AA0317	23.864	5.937	4.464	235.718	MN18101435	26.051	7.93	4.019	156.437
MN12AA0117	26.345	11.933	8.937	462.829	MN13AA0811	43.527	15.29	5.686	868.641
MN12AA5615	26.272	7.399	3.405	166.013	MN13AA1019	38.022	17.96	8.277	1756.653
MN12AA0919	22.86	17.451	10.758	947.922	MN13AA1118	46.792	6.233	3.998	285.192
MN12AA5614	17.528	7.606	3.003	170.465	MN13AA1016	46.01	14.278	6.962	1439.383
MN12AA0915	27.448	23.421	9.452	1882.444	MN18031118	19.234	14.27	5.651	378.936
MN12AA6015	34.595	17.562	5.135	638.828	MN13AA1112	47.946	10.388	8.336	1201.244
MN10AA1008	30.003	9.491	6.697	490.705	MN13AA1126	40.094	18.601	5.692	1017.777
MN10AA1805	19.489	14.823	4.693	416.453	MN18031122	23.571	8.595	2.537	153.816
MN19061804	27.362	15.579	6.029	832.246	MN18031220	37.869	10.425	10.326	1090.691
MN12AA6511	26.234	9.249	6.175	352.032	MN18031010	35.956	11.027	4.066	449.146
MN12AA5612	15.101	11.072	3.675	194.788	MN13AA1018	41.911	16.909	8.735	1579.148
MN10AA0209	27.261	10.899	5.155	400.246	MN18031317	25.452	8.718	6.029	320.213
MN10AA0712	19.625	9.874	6.136	380.176	MN18031009	33.422	13.839	7.274	783.333
MN19063109	22.346	12.387	6.362	371.91	MN13AA0809	53.769	15.834	7.608	2375.836
MN10AA0711	30.66	12.91	4.818	519.736	MN18071716	25.454	7.571	4.587	279.188
MN12AA0215	32.937	12.442	7.508	720.671	MN18032104	23.834	17.681	9.198	1044.654
MN12AA6314	28.562	15.839	6.502	699.964	MN18071120	31.055	15.882	7.004	662.885
MN10AA1010	16.239	11.023	6.559	295.66	MN18032108	28.633	5.826	2.883	151.117

Table 2 – continued from previous page

Specimen	Length	Width	Depth	Volume	Specimen	Length	Width	Depth	Volume
MN12AA0411	31.737	12.879	6.622	758.229	MN18101444	20.979	6.909	2.226	107.891
MN19063106	28.63	11.598	3.935	232.694	MN18032008	29.842	18.303	9.157	1765.071
MN12AA5617	23.727	15.467	9.06	966.545	MN13AA1214	41.108	12.095	8.19	1257.778
MN10AA0610	27.415	8.145	3.991	240.039	MN18031225	32.056	10.124	9.354	791.267
MN12AA1116	24.842	14.14	9.774	666.935	MN18031006	53.135	18.687	10.577	2619.149
MN12AA0123	21.224	12.825	9.007	699.195	MN18101434	23.77	6.69	6.32	329.657
MN12AA5811	29.844	15.183	7.529	641.757	MN18071921	35.788	14.466	7.435	1317.977
MN10AA0210	25.283	6.629	3.99	194.405	MN18031312	42.503	8.494	5.833	446.903
MN10AA2010	30.365	8.36	4.733	299.059	MN18072332	26.565	15.561	7.192	826.387
MN19063115	21.986	5.813	3.412	102.342	MN18101426	22.616	11.717	5.996	533.429
MN10AA0313	14.471	8.099	6.466	229.285	MN18030422	18.475	12.775	9.409	397.766
MN10AA0807	29.878	14.254	10.434	957.62	MN18101418	33.739	11.413	8.674	1038.295
MN12AA0210	27.036	22.196	8.254	1519.145	MN13AA1218	40.041	12.752	7.654	679.413
MN12AA0303	35.214	15.218	6.079	986.702	MN18101430	16.282	11.1	4.275	188.732
MN12AA0917	28.296	15.514	7.499	724.889	MN18031113	41.429	13.491	8.463	1240.607
MN19063008	23.561	12.359	3.818	211.276	MN18031015	15.344	8.787	3.844	142.684
MN12AA6012	32.034	10.51	8.326	684.972	MN18101425	19.321	13.123	3.675	380.996
MN19063116	17.822	8.42	5.514	200.92	MN18071707	18.506	14.904	4.312	354.33
MN10AA1012	24.226	18.945	10.223	1440.861	MN18071828	25.017	9.525	7.47	452.388
MN19063108	29.107	14.171	4.784	381.194	MN18071622	25.679	18.41	8.625	737.625
MN12AA0304	27.347	15.902	6.204	587.8	MN18031221	51.256	10.68	6.406	1177.777
MN12AA6410	23.966	14.126	6.653	553.39	MN18032105	18.646	12.344	7.685	501.346
MN19063009	19.724	8.826	4.637	273.877	MN18072023	33.455	15.113	6.534	976.879
MN10AA1009	25.006	14.569	5.227	539.47	MN18071709	24.16	13.093	5.127	315.927
MN10AA0812	27.329	10.812	7.585	544.398	MN18031316	27.966	11.364	5.61	386.3
MN10AA0115	29.8	9.549	5.438	320.717	MN18071706	25.926	11.211	7.48	450.201
MN19060607	20.352	19.186	8.302	839.107	MN18031314	21.386	15.805	4.803	601.253
MN12AA0514	28.186	16.629	6.531	954.772	MN18072327	28.36	22.839	8.492	1255.46
MN12AA6513	26.291	12.576	6.746	619.991	MN18072324	34.355	18.426	5.016	947.673
MN12AA6108	26.337	16.828	7.498	1073.584	MN18032102	23.117	21.106	9.182	1232.031
MN12AA5813	23.008	13.499	7.619	454.764	MN18031227	21.715	7.141	4.22	217.969
MN12AA0515	17.236	14.163	4.056	304.083	MN18101429	16.773	10.35	6.993	260.86
MN10AA0911	31.235	11.944	6.9	591.738	MN18072325	36.456	20.618	5.507	1376.638
MN12AA6510	23.801	16.817	5.383	665.613	MN18031315	25.893	9.448	4.803	320.537
MN10AA0311	26.436	13.289	5.03	466.562	MN13AA1017	48.567	14.447	7.656	936.901
MN12AA0918	31.718	13.976	7.642	784.166	MN18101417	36.716	14.062	9.213	1107.786
MN19060610	21.765	9.927	3.98	279.657	MN18031219	29.303	21.366	6.857	1130.555
MN19063011	16.04	10.469	5.608	243.31	MN18071122	27.49	15.458	2.527	285.361
MN10AA0608	35.917	9.397	5.5	667.07	MN18032103	23.218	20.43	6.722	787.223
MN12AA6111	21.004	19.344	7.881	998.377	MN18032110	21.443	10.156	5.515	384.499
MN10AA0406	24.954	9.982	7.1	539.783	MN18101433	25.897	7.402	3.474	218.235
MN19060608	22.387	11.139	5.624	415.31	MN18031117	24.614	10.533	4.947	328.555
MN12AA5616	32.194	16.324	6.249	800.54	MN13AA0916	40.299	12.751	7.98	935.345

Table 2 – continued from previous page

Specimen	Length	Width	Depth	Volume	Specimen	Length	Width	Depth	Volume
MN10AA0510	31.338	9.043	4.383	370.775	MN18072338	18.43	10.635	3.293	154.013
MN19064211	44.222	10.019	5.132	764.285	MN18031228	15.899	13.577	3.965	198.155
MN18060721	32.039	15.515	4.791	411.269	MN18032109	18.41	14.151	6.371	353.231
MN19063907	45.25	12.768	9.485	704.769	MN13AA0914	44.094	15.155	7.723	1159.545
MN18061013	25.637	14.89	7.658	771.184	MN18071616	35.664	19.918	10.324	2142.372
MN19080602	22.936	16.227	6.269	532.134	MN18031311	51.012	10.373	6.08	744.401
MN19080605	18.093	15.76	4.458	266.76	MN18101312	30.018	11.185	5.837	454.821
MN19063707	16.175	10.47	5.643	304.938	MN18101436	25.747	10.13	4.972	136.763
MN18061210	35.504	8.921	5.884	497.017	MN18101421	32.134	10.893	3.193	232.477
MN18060724	30.641	10.877	4.962	523.372	MN18031115	37.364	11.745	4.865	588.255
MN18060712	47.872	18.602	8.72	1542.807	MN18072713	45.582	7.089	4.138	399.65
MN18061112	26.72	18.141	6.441	847.411	MN18110718	28.988	12.077	7.293	659.916
MN18061312	24.221	14.899	5.11	502.528	MN18101310	27.731	10.4	5.248	314.071
MN18060719	24.647	16.413	5.477	475.871	MN18072333	34.917	10.386	6.243	589.971
MN19065013	39.325	19.28	5.094	941.946	MN18110231	30.673	16.24	8.253	1238.455
MN18061110	21.57	14	5.554	400.948	MN18072714	34.237	6.715	5.614	497.032
MN18060808	35.563	16.643	7.468	1112.851	MN18110714	32.997	15.793	6.965	968.772
MN18060731	20.196	6.585	2.424	95.928	MN18072717	28.257	6.994	4.378	192.011
MN19063708	13.392	10.21	5.261	196.073	MN18072408	37.952	11.759	7.742	696.915
MN18061211	26.269	13.814	6.164	679.657	MN18071917	45.805	19.263	6.631	1375.059
MN18061016	20.099	13.108	5.612	331.972	MN18100206	30.124	16.312	8.682	790.601
MN19064109	25.705	12.642	5.27	370.173	MN18110235	33.987	15.718	7.848	1102.612
MN19063905	42.665	20.147	10.505	1631.654	MN18071821	40.064	10.222	3.716	586.429
MN19064409	16.111	9.99	5.057	203.697	MN18110239	30.781	11.958	5.202	620.498
MN18061613	23.206	13.06	5.496	370.377	MN18110237	31.924	21.042	3.924	640.565
MN18061308	29.35	15.55	5.804	677.627	MN18072014	46.19	22.09	9.115	2271.656
MN18061416	16.364	11.159	8.553	496.792	MN18072021	37.137	15.015	10.606	1140.363
MN18060720	32.776	13.913	5.543	794.299	MN18110712	30.911	21.065	7.407	1469.755
MN19064008	15.133	5.181	2.947	54.141	MN18101410	53.182	19.027	10.019	3250.483
MN18061310	30.463	17.457	4.433	461.896	MN18072317	43.213	17.616	11.211	1987.661
MN19065310	35.924	13.795	8.14	985.281	MN18101414	47.913	14.95	6.656	1738.466
MN19065309	31.236	15.557	7.561	1094.153	MN18110217	44.107	18.45	8.022	2827.937
MN19063609	16.527	13.002	3.683	155.55	MN18032007	52.234	13.747	7.022	1398.218
MN19064106	36.943	13.402	8.039	897.63	MN18072409	35.605	8.344	5.171	373.001
MN18061111	22.241	14.693	5.751	463.868	MN18071825	30.933	9.133	6.548	431.886
MN19063808	21.738	9.056	8.042	306.074	MN18072025	30.484	11.822	6.619	813.854
MN19065023	16.577	6.887	5.158	194.368	MN18110222	52.64	12.415	8.638	1651.083
MN19065022	17.922	6.18	4.951	144.167	MN18101412	48.583	18.725	10.736	1691.711
MN18061215	33.789	8.211	7.072	288.987	MN18110221	38.264	18.696	5.683	1417.023
MN18061415	29.126	10.17	5.677	354.717	MN18110227	53.309	15.43	9.631	1784.231
MN19064308	25.527	9.12	4.574	251.172	MN18072321	37.675	18.51	7.48	2012.825
MN19063805	41.334	17.323	8.11	1303.353	MN18031917	41.44	12.457	5.513	796.411
MN19064808	22.567	10.039	4.168	206.918	MN18071116	33.979	20.027	5.958	1094.604

Table 2 – continued from previous page

Specimen	Length	Width	Depth	Volume	Specimen	Length	Width	Depth	Volume
MN19063909	34.652	6.186	2.883	156.634	MN18072611	45.816	17.463	8.821	1636.847
MN19065021	23.334	7.209	3.619	112.719	MN18072715	35.397	4.859	3.967	173.971
MN18061011	34.656	17.96	10.157	1153.04	MN18110244	24.162	11.244	5.409	375.88
MN19064105	28.013	18.6	10.717	1018.46	MN18110620	31.664	17.243	6.603	991.385
MN18061214	18.547	10.716	7.26	515.489	MN18110240	22.756	12.884	7.234	603.252
MN19064005	17.267	11.481	3.19	155.882	MN18032107	32.99	9.012	3.79	252.125
MN18060714	35.316	15.403	7.587	967.393	MN18072406	31.507	13	5.717	822.414
MN18060725	32.423	10.204	7.052	501.591	MN18101316	20.703	11.661	5.915	210.61
MN19064809	12.904	9.424	4.369	208.061	MN18072320	42.094	22.713	7.491	1419.834
MN19064208	30.128	13.038	6.619	805.839	MN18071710	33.876	14.964	3.593	309.85
MN19063611	13.516	8.115	2.796	75.877	MN18072102	49.794	17.487	8.106	1935.836
MN18061414	26.149	10.965	7.81	649.357	MN18072318	42.68	19.987	10.1	1775.151
MN19064110	14.554	8.682	2.949	76.118	MN18071415	30.046	22.338	8.65	1954.488
MN19064408	26.824	7.839	3.614	161.333	MN18071820	39.101	10.397	5.369	672.311
MN19064806	19.624	10.45	4.097	265.042	MN18071918	53.172	18.563	8.007	2508.216
MN19064006	17.734	7.87	6.069	225.75	MN18072903	35.967	13.762	6.79	1168.003
MN19063606	26.555	10.033	4.003	429.747	MN18110243	27.035	7.856	7.562	565.308
MN19065019	24.237	8.081	3.868	231.401	MN18072040	40.302	12.831	8.2	1353.256
MN18061612	32.801	11.535	3.664	296.268	MN18110228	32.354	21.581	6.826	1713.047
MN18061109	31.25	10.755	5.933	416.946	MN18072316	51.954	18.336	10.419	1497.266
MN18061615	22.674	7.957	3.315	202.293	MN18072017	36.299	19.593	9.525	1431.743
MN19065017	18.618	14.923	4.602	274.101	MN18110505	19.842	10.556	8.27	337.864
MN18061209	21.451	15.078	10.326	903.37	MN18110623	25.693	13.606	5.553	546.279
MN18061313	22.922	14.678	5.386	451.232	MN18031918	33.845	15.089	7.501	729.051
MN19064912	24.768	10.685	4.979	283.661	MN18071123	20.746	9.993	6.007	270.539
MN19064007	16.664	6.948	3.137	74.684	MN18110108	42.852	19.516	11.245	1315.358
MN18061212a	21.46	14.134	6.857	491.088	MN18031921	27.258	9.818	5.092	242.844
MN18061418	23.915	7.194	4.523	242.424	MN18072502	42.33	20.008	11.113	2483.398
MN19064306	26.018	12.317	8.426	570.744	MN18101311	19.388	13.385	5.063	393.766
MN18061208	29.369	18.669	5.945	809.858	MN18110230	28.437	16.169	9.516	1329.433
MN19063504	30	8.923	4.738	397.667	MN18101309	22.949	15.429	5.561	654.445
MN19064407	22.454	7.453	5.553	317.307	MN18072901	41.542	20.149	8.446	1910.117
MN19063605	32.629	14.475	10.674	578.819	MN18072016	37.293	20.933	8.853	1278.503
MN19064104	47.381	18.851	9.887	1797.609	MN18071414	37.138	10.639	3.173	236.491
MN18060729	17.504	13.889	3.832	211.336	MN18031111	48.443	17.37	5.723	1224.138
MN18061107	26.44	16.089	6.113	581.628	MN18072503	33.28	15.898	7.132	1462.477
MN19063706	18.519	11.393	8.675	406.784	MN18072902	31.134	19.477	7.394	1758.917
MN18060718	31.169	14.812	5.509	520.796	MN18071625	28.185	9.95	4.461	408.87
MN18061614	26.957	11.204	5.073	349.039	MN18101307	35.735	17.318	6.364	1002.776
MN18061417	26.543	6.885	5.323	313.253	MN18072030	23.78	13.733	4.887	356.263
MN19064213	30.415	12.889	3.792	492.148	MN18101413	42.607	15.129	8.574	1557.876
MN18061212b	15.904	15.092	7.625	619.893	MN18072908	28.227	9.617	6.259	471.762
MN19064909	32.802	13.749	8.218	678.575	MN18071117	37.122	12.96	2.923	235.251

Table 2 – continued from previous page

Specimen	Length	Width	Depth	Volume	Specimen	Length	Width	Depth	Volume
MN19063713	14.518	5.753	3.972	91.459	MN18072029	27.149	10.298	8.038	631.28
MN19064807	19.967	15.842	7.165	261.406	MN18032101	41.785	12.495	9.41	1226.985
MN19063807	28.87	11.138	6.002	472.699	MN18072319	50.294	15.048	6.48	1483.981
MN18061617	16.457	12.529	5.647	196.654	MN18110234	34.78	13.108	9.297	1053.538
MN19064108	30.148	7.932	4.315	292.365	MN18071701	44.436	21.362	8.208	1310.911
MN19065014	39.317	11.918	5.76	831.704	MN18110713	32.859	16.159	9.462	1661.619
MN19064405	28.336	8.049	5.259	353.783	MN18110238	31.712	12.74	7.434	796.164
MN18061309	29.326	13.5	4.758	465.994	MN18101317	19.851	9.58	4.345	223.267
MN19063403	20.158	10.061	5.081	279.943	MN18071922	40.775	16.752	6.802	522.031
MN18061014	25.031	14.485	7.094	555.017	MN18110241	27.855	12.271	3.88	393.662
MN18060734	15.689	8.735	3.354	126.78	MN18072018	43.45	12.991	9.086	1523.929
MN19060805	41.603	17.45	7.551	651.917	MN18101419	39.08	8.35	5.344	426.178
MN19065311	35.516	18.468	6.789	1031.649	MN18110622	28.852	7.593	6.193	501.866
MN19064403	34.561	14.041	6.352	832.092	MN18101308	24.784	20.969	6.967	795.367
MN18060807	35.037	9.706	8.321	706.338	MN18101313	23.681	10.651	4.698	189.161
MN19065312	29.048	15.415	10.009	896.685	MN18101415	43.282	13.35	5.446	1099.051
MN19064107	29.449	12.351	5.821	451.974					